ARTICLE

High Thermal Conductivity of Submicrometer Aluminum Nitride Thin Films Sputter-Deposited at Low Temperature

Christopher Perez,* Aaron J. McLeod, Michelle E. Chen, Su-in Yi, Sam Vaziri, Ryan Hood, Scott T. Ueda, Xinyu Bao, Mehdi Asheghi, Woosung Park, A. Alec Talin, Suhas Kumar,* Eric Pop, Andrew C. Kummel, and Kenneth E. Goodson*

Read Online

ACCESS | Metrics & More | Article Recommendations | Supporting Information

ABSTRACT: Aluminum nitride (AlN) is one of the few electrically insulating materials with excellent thermal conductivity, but high-quality films typically require exceedingly hot deposition temperatures (>1000 °C). For thermal management applications in dense or high-power integrated circuits, it is important to deposit heat spreaders at low temperatures (<500 °C), without affecting the underlying electronics. Here, we demonstrate 100 nm to 1.7 μm thick AlN films achieved by low-temperature (<100 °C) sputtering, correlating their thermal properties with their grain size and interfacial quality, which we analyze by X-ray diffraction, transmission X-ray microscopy, as well as Raman and Auger spectroscopy. Controlling the deposition conditions through the partial pressure of reactive N_2, we achieve an ∼3× variation in thermal conductivity (∼36−104 W m^{-1} K^{-1}) of ∼600 nm films, with the upper range representing one of the highest values for such film thicknesses at room temperature, especially at deposition temperatures below 100 °C. Defect densities are also estimated from the thermal conductivity measurements, providing insight into the thermal engineering of AlN that can be optimized for application-specific heat spreading or thermal confinement.

KEYWORDS: thermal conductivity, aluminum nitride, back end of line, thermal transport, sputter deposition, low temperature, power electronics
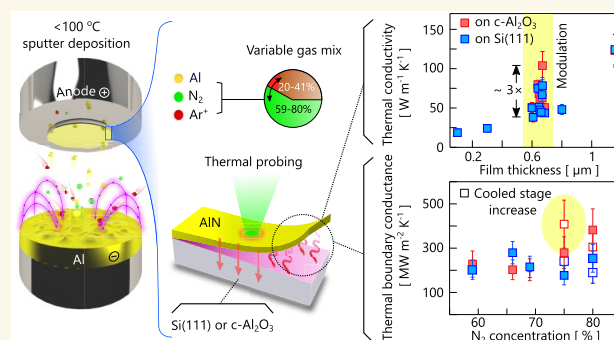
INTRODUCTION

Heat generation impedes the performance and longevity of nearly all modern electronic devices.[1−3] This is especially true in high-density integrated circuits[4] and power or radio-frequency (RF) electronics,[3,5] where elevated temperatures reduce transistor performance, increase leakage, and ultimately diminish device lifetimes.[6,7] A mere 5 °C increase in temperature above the optimum operating range can halve the lifetime of some devices.[7,8] Thermal management could be achieved by actively tuning heat flow and managing thermal transients, e.g. with the use of emerging thermal transistors and diodes.[9−11] Passive approaches involve simply using thin films to block or route heat away from hot spots in electronics. Such heat spreaders must have high thermal conductivity, but they must often be electrical insulators to prevent cross-talk between components—a set of properties that are common to only a few materials, such as aluminum nitride (AlN), boron nitride (BN), and diamond.

In particular, AlN has attracted much attention due to its large band gap (roughly 6.1 eV)[12,13] and bulk thermal conductivity (approximately 340 W m^{-1} K^{-1} at room temperature, or 85% the thermal conductivity of copper).[14−17] Indeed, bulk-like thermal conductivities have been demonstrated for AlN films on the order of hundreds,[16] tens,[18] and a few micrometers[19−21] in thickness, but such films are typically deposited at over 1200 °C. High temperatures are incompatible with many requirements of fabricating integrated circuits, where low-temperature (e.g., <500 °C for <2 h) deposition is required for back-end-of-line (BEOL) processes.[22−24] More-
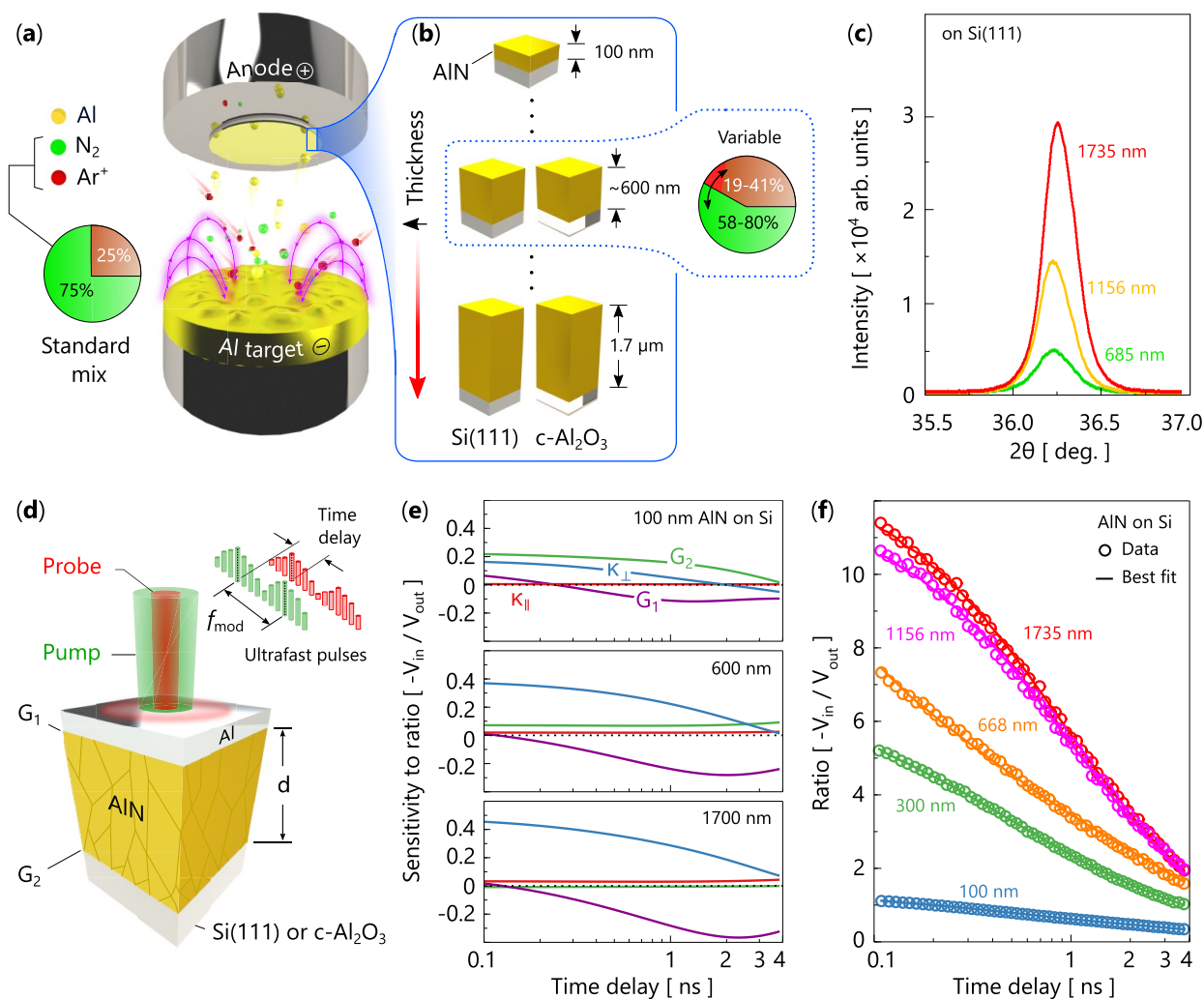
Figure 1. Experimental overview. (a) Illustration of our balanced DC magnetron sputtering deposition of AlN films using a standard sputter gas mix of 25% Ar and 75% N_2. **(b)** Schematic of the AlN film thickness variations explored in this work, along with their deposition on both Si(111) and c-Al$_2$O$_3$. The ~600 nm films are used to highlight the tuning of thermal conductivity by manipulating the sputtering gas composition. **(c)** Bragg−Brentano X-ray diffraction (XRD) spectra shown for the AlN films of various thicknesses deposited on Si(111), the results of which are used to estimate the grain size. **(d)** Simplified schematic of the TDTR measurement of the multilayer stack of materials used to determine thermal properties of the AlN films via detection of the sample response to periodic heating at a modulation frequency (f_{mod}). **(e)** Sensitivity of the TDTR ratio ($-V_{in}/V_{out}$) to the cross- and in-plane thermal conductivity ($\kappa_\perp/\kappa_\parallel$), Al/AlN thermal boundary conductance (G_1), and AlN/substrate thermal boundary conductance (G_2). **(f)** Characteristic model fits for the AlN films on Si ranging from $d \approx 100$ to 1735 nm in thickness. Input properties for these calculations are provided in Section S5 of the Supporting Information.

over, integrated electronics would also benefit from thinner, microscale films of AlN, whose thermal conductivity has not been optimized and whose thermal limits are poorly understood. Devices fabricated with AlN heat spreaders, for example, can be complex and the literature remains unclear as to the dominant phonon scattering mechanisms in submicrometer versions of these materials.[25,26]

In this work, we demonstrate AlN films deposited by low-temperature (<100 °C) DC reactive balanced magnetron sputtering, with thicknesses ranging from 100 nm to 1.7 μm. The thermal conductivity of the films is determined by time-domain thermoreflectance (TDTR) and is correlated with microstructural properties, such as grain size and morphology, as determined by X-ray diffraction (XRD) and transmission electron microscopy (TEM), respectively. For films around 600 nm in thickness, we find the cross-plane thermal conductivity can be tuned by a factor of 3 by controlling the sputtering gas composition during deposition, with the upper

end (~104 W m^{-1} K^{-1}) representing one of the highest values for this thickness at room temperature and at such low, BEOL-compatible deposition temperatures. Comparing these results with models based on the Boltzmann transport equation (BTE) for phonons shows that defect densities are being modulated by over an order of magnitude to produce the variation in thermal conductivity in our AlN films.

RESULTS AND DISCUSSION

AlN films were deposited using balanced DC sputtering,[27,28] as depicted in Figure 1a. Two series of AlN films were deposited (Figure 1b); the first used a standard gas composition of 25% Ar and 75% N_2 with film thicknesses of 685, 1156, and 1735 nm on both Si(111) and c-Al$_2$O$_3$ substrates shown in Figure 1a. The data for these films are summarized in Table 1, and deposition details can be found in Section S1 in the Supporting Information.

Table 1. Thickness, thermal conductivity, AlN (002) diffraction eak width, and estimated grain size (GS) for films of varied thickness deposited using a 75% N_2 and 25% Ar mixture on a non-chilled sample stage

substrate	d (nm)	κ (W m^{-1} K^{-1})	(002) FWHM (deg)	GS (nm)
Si(111)	100	18.7 ± 4.6	0.998	9.0
Si(111)	300	25.5 ± 4.7	0.660	13.2
Si(111)	647	51.1 ± 5.0	0.260	33.6
Si(111)	800	48.1 ± 6.4	0.620	14.0
Si(111)	1156	124.3 ± 19.4	0.194	45.2
Si(111)	1735	125.7 ± 21.4	0.186	47.0
c-Al$_2$O$_3$	647	68.1 ± 8.6	0.207	42.2
c-Al$_2$O$_3$	1156	122.8 ± 20.4	0.195	44.8
c-Al$_2$O$_3$	1735	118.9 ± 18.4	0.152	57.5

The second series of films approximately 600 nm in thickness were grown to demonstrate the tunability of the room-temperature (RT) thermal conductivity (κ) by manipulating the sputtering gas composition. Deposition details for these films can be found in Table 2 using both Si(111) and c-sapphire substrates with gas compositions varying from 19% to 41% Ar and from 58% to 80% N_2, shown in Figure 1b. Two of the samples in this series were deposited using a stage cooled to 10 °C. Additional films for this series were deposited using Kr in place of Ar, with details presented Section S2 in the Supporting Information. The films were characterized by Bragg−Brentano X-ray diffraction (XRD), an example of which is shown for the set of films with varied thickness in Figure 1c (Section S3 in the Supporting Information). In addition, high-resolution transmission electron microscopy (HR-TEM) was performed on the most thermally dissimilar samples. Time domain thermoreflectance (TDTR), as seen in Figure 1d−f, was performed on all films to measure their cross-plane thermal conductivity. Raman spectroscopy was also carried out to assess the film quality by means of characteristic E_2^2 modes and narrow full-width at half-maximum (FWHM) values,[29] shown in Section S4 of the Supporting Information.

A schematic of the AlN film specimens measured in this work is displayed in Figure 1d, consisting of an aluminum (Al) optothermal transducer, the AlN film, and a Si(111) or c-Al$_2$O$_3$ substrate. Thermal properties were determined by TDTR (Section S5 in the Supporting Information), an optical pump−probe technique described extensively in our prior works.[30−32] In TDTR, an ultrafast laser is used to both induce (pump) and monitor (probe) modulated heating on the surface of the sample as a function of pump−probe time delay. The thermal conductivity and thermal boundary conductances are then determined by fitting the intensity of the ratio $(-V_{in}/V_{out})$ signal of the reflected probe laser to a three-dimensional (3D) heat diffusion model for a multilayer stack of materials. Given the measurement conditions provided in Materials and Methods, the measurement is primarily sensitive to cross-plane thermal conductivity ($\kappa = \kappa_\perp$), as shown by the sensitivity calculations displayed in Figure 1e, which displays the sensitivity of the TDTR signal to the relevant properties for 100−1700 nm thick AlN films on a Si(111) substrate (see Section S6 in the Supporting Information). This is attributed to the disparity between the root-mean-square (RMS) average laser spot radius (w_{RMS}) and the in-plane thermal penetration depth that induces one-dimensional (1D) heat transfer.[33]

The high thermal conductivity and submicrometer thicknesses of these AlN films complicate the extraction of thermal properties and thus warrant an optimization approach. As the thermal penetration depth into the sample becomes comparable to the film thicknesses, the thermal boundary conductances on either side of the film increasingly influence the total thermal resistance of the measured system. As seen in Figure 1e, both the Al/AlN and AlN/Si interfaces (G_1 and G_2, respectively) contribute prominently to the thermal response for a 100 nm AlN film, while the AlN/Si interface becomes insensitive with a 1700 nm AlN film, i.e. it is thermally thick. For the ∼600 nm films, however, the contribution of the AlN/Si interface is diminished but still significant. As shown in Section S7 of the Supporting Information, a global optimization sweeping the typical range of semiconductor-dielectric interfaces[34] was performed to extract the thermal boundary conductances and intrinsic conductivities that provided the best fit to our thermal model with the lowest uncertainty, examples of which are shown in Figure 1f. Films on c-Al$_2$O$_3$ were analyzed in a similar manner but with slightly greater uncertainties in the thermal interfaces due to the

Table 2. Deposition conditions, film thicknesses, thermal conductivities, AlN (002) diffraction peak full-width at half-maximum (FWHM) Values, and estimated grain size (GS) for the measured films deposited using various sputtering gas compositions

substrate	cooled?	N_2 (%)	Ar (%)	d (nm)	κ (W m^{-1} K^{-1})	(002) FWHM (deg)	GS (nm)
c-Al$_2$O$_3$		59	41	645	48.3 ± 5.0	0.262	33.3
c-Al$_2$O$_3$		66	34	607	36.1 ± 3.8	0.303	28.8
c-Al$_2$O$_3$		69	31	600	50.8 ± 6.2	0.185	47.2
c-Al$_2$O$_3$		75	25	685	50.6 ± 3.3	0.168	52.0
c-Al$_2$O$_3$	Y	75	25	670	103.9 ± 17.9	0.126	69.3
c-Al$_2$O$_3$		80	20	639	74.9 ± 6.4	0.215	40.6
c-Al$_2$O$_3$	Y	80	20	668	62.9 ± 6.9	0.222	39.4
Si(111)		59	41	645	43.2 ± 4.3	0.242	36.1
Si(111)		66	34	607	38.1 ± 3.2	0.198	44.1
Si(111)		69	31	600	50.2 ± 5.4	0.205	42.6
Si(111)		75	25	685	43.7 ± 4.2	0.222	39.3
Si(111)	Y	75	25	670	78.5 ± 10.3	0.168	52.0
Si(111)		80	20	639	79.8 ± 5.5	0.177	49.3
Si(111)	Y	80	20	668	66.9 ± 8.4	0.185	47.2

increased contribution of the substrate to the probed thermal resistance.[35]

The measured cross-plane thermal conductivities of our AlN films are displayed in Figure 2a and compared to values from
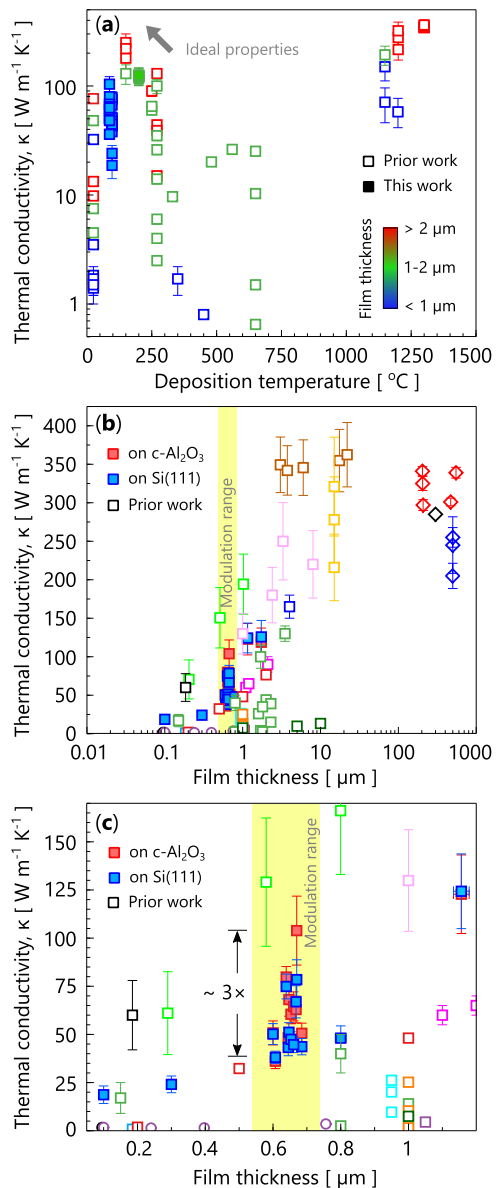

Figure 2. Room-temperature cross-plane thermal conductivity of our AlN films (filled square symbols) as functions of (a) deposition temperature and (b) thickness, compared to results from the literature.[18,19,29,34,36−42] In (b), diamond symbols are single-crystal samples: Slack[43] (black), Rounds[44] (red), and Xu[16] (blue). Square symbols are for polycrystalline films: Kuo[19] (orange), Jacquot[45] (light blue), Zhao[36] (purple), Choi[37] (red), Pan[39] (cyan), Aissa[40] (pink), Duquenne[38] (green), Alvarez-Escalante[42] (light green), Bian[41] (dark green), Yalon[29] (black), Cheng[18] (yellow), Koh[20] (brown), and Bellerk[46] (magenta). Round symbols correspond to amorphous thin films: Zhao[36] (purple) and Gaskins[34] (black). We note that the reported thermal conductivities are either isotropic or cross-plane to make for a fair comparison to our results and that nearly all films have deposition temperatures much greater than ours. The yellow shaded region marks the range of thicknesses wherein we demonstrate the modulation of thermal conductivity via a structure−processing−property relationship, magnified in (c) to show a ∼3× change.

the literature[18−20,29,34,36−41] as a function of deposition temperature. Red, green, and blue symbols mark films greater than 2 μm, 1−2 μm, and less than 1 μm in thickness, respectively. The results of this study represent some of the highest reported thermal conductivities for submicrometer thin AlN films when considering the low deposition temperature of under 100 °C. The substrates were not actively heated during deposition, though a thermocouple placed under the substrate holder allowed for temperature monitoring. With initial stage cooling to 10 °C, temperature saturation due to plasma exposure during deposition occurred at 70 °C, lower than the 90−100 °C observed for samples deposited without stage cooling. In contrast, most chemical and physical deposition methods rely on heating substrates to several hundred degrees Celsius to effectively crystallize deposited material, producing films with greater thermal conductivity.

The thermal conductivities of our AlN films sputtered at BEOL-compatible temperatures are compared with results from other studies as a function of film thickness in Figure 2b; these results are represented by filled symbols that are either red or blue, for films on c-Al$_2$O$_3$ and Si(111), respectively. In the submicrometer regime, the high thermal conductivity of our films indicates decreased defect density and reduced boundary scattering effects that typically plague nonepitaxial thin films, regardless of deposition technique. Indeed, minimizing defect densities and promoting the growth of larger grains is the primary focus of thin-film synthesis in electronic heat-spreading applications.[47,48] The yellow shaded region in Figure 2b shows the range of thermal conductivities achieved in this work by varying the sputtering deposition conditions. Figure 2c magnifies this region to show that the AlN thermal conductivity for the set of ∼600 nm films can range from ∼36 to ∼104 W m^{-1} K^{-1}: a nearly 3-fold change.

The modulation of thermal conductivity via a structure−processing−property relationship in these AlN films by tuning the sputtering gas composition was employed to understand the underlying mechanisms of improvement. Figure 3a plots the thermal conductivity with respect to the N$_2$ gas concentration of the ∼600 nm films on both c-Al$_2$O$_3$ and Si(111) in red and blue, respectively, with open symbols representing samples deposited using a cooled stage. We note that the balance gas for sputtering is Ar such that it comprises the full gas mixture, i.e., Ar(%) = 1 − N$_2$(%). Deposition on a noncooled stage with lower N$_2$ concentrations of 59−75% yielded lower thermal conductivity values ≤ 50 W m^{-1} K^{-1}. Conversely, an 80% N$_2$ deposition environment produced the most thermally conductive film among those that were not cooled. This is in contrast to work by Shinoda et al.,[49] who implemented a low N$_2$ concentration of 30% to produce films of high crystallinity, though with RF reactive magnetron sputtering and substrate temperatures exceeding 900 °C. In contrast, Kumada et al.[50] reported optimal N$_2$ concentrations of 40−50%, but with lower substrate temperatures of approximately 500 °C.

The general trend between higher N$_2$ concentrations and lower substrate temperatures, in the literature and in this work, highlights the complex interplay between process parameters: it is possible that at lower deposition temperatures, higher concentrations of N$_2$ are necessary to ensure complete nitridation of the deposited material. Further obscuring these relationships is the interplay of throw distance and ion mean free path, which itself is dependent upon a combination of pressure, applied power, and magnetic configuration of the
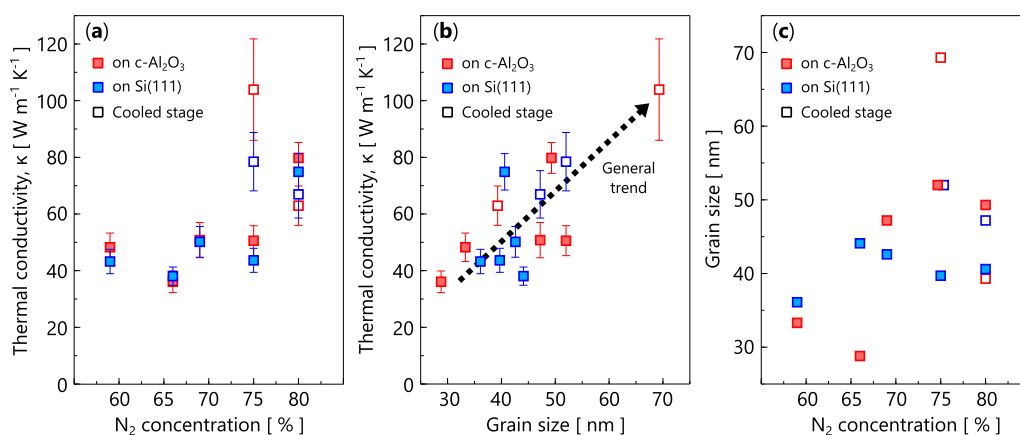
Figure 3. Correlations among thermal conductivity, grain size, and gas composition for ~600 nm AlN films. (a) Thermal conductivity with respect to N_2 concentration and (b) grain size. The relationship between grain size and thermal conductivity is consistent with the importance of grain boundary scattering on thermal transport. Open squares represent films deposited on a cooled stage and exhibit the largest thermal conductivities. (c) Grain size with respect to the N_2 concentration. Note that the data at 75% N_2 concentration are slightly offset laterally for clarity.
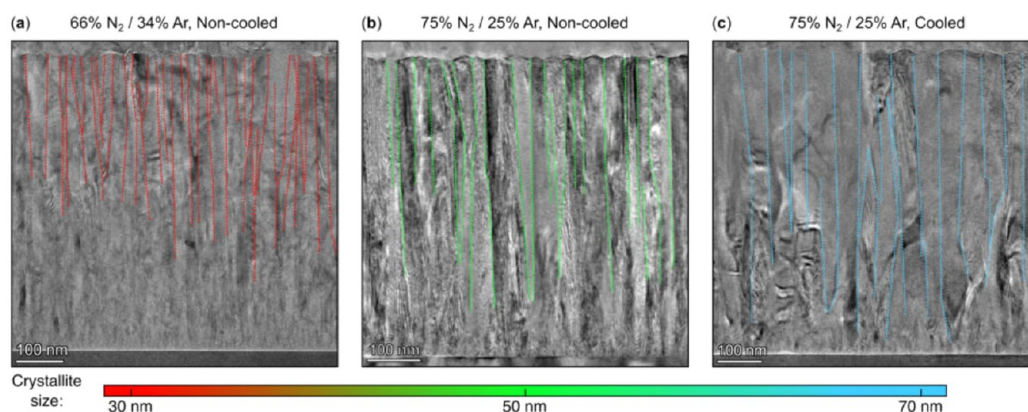
Figure 4. Transmission electron micrographs showing the full grain morphology for three sputtered films on c-Al_2O_3 using different conditions: (a) 66% N_2 and 34% Ar on a nonchilled stage, (b) 75% N_2 and 25% Ar without stage cooling, and (c) 75% N_2 and 25% Ar with the stage cooled to 10 °C throughout deposition. Grain boundaries are outlined to guide the eye.

sputtering equipment. Altering these parameters, directly or indirectly, affects the extent to which the reaction occurs in the plasma as well as the energetics of species bombarding the growth surface.[51] Careful tuning is necessary to ensure that the structure of the deposited material is tailored to enhance the properties of the material for the intended application.

Surprisingly, depositions with a cooled stage produced the most thermally conductive films in this work and some of the highest values reported in the field. Average grain sizes (GSs), are provided in Figure 3b, estimated using the FWHM of the AlN (002) diffraction peak and the Debye−Scherrer equation, revealing a positive correlation between grain size and thermal conductivity. Such a trend is consistent with decreased phonon scattering at grain boundaries, which is often the dominant scattering mechanism in dielectrics and semiconductors.[52] For clarity, these data are combined in Figure 3c to show the generally positive correlation among thermal conductivity, nitrogen content, and average grain size. It is well established that increasing the substrate temperature enhances surface migration and thus, crystalline quality. However, increased compressive stress at the AlN/substrate interface can occur during the postdeposition cooling process,[50] which can play a major role in determining overall crystallinity.[53] It is interesting to note that the stage-cooled films deposited with an 80% N_2

gas concentration become slightly less thermally conductive than their uncooled counterparts, suggesting an optimization among the aforementioned effects. Thermal measurements of AlN films deposited with Kr gas in place of Ar were also performed (see Section S2 in the Supporting Information) but demonstrated only moderate improvement with stage cooling.

TEM was performed on three films deposited on c-Al_2O_3 to gain insight into the microstructural features that influence transport. Figure 4 shows cross sections of two films deposited without stage cooling: (a) the most thermally insulating film deposited using 66% N_2 and (b) a film deposited using 75% N_2 with a larger thermal conductivity value. Grain boundaries are outlined to reveal a noticeable difference in their size and frequency, in agreement with both the estimated grain sizes and the thermal conductivity values (~38 and ~50 W m^{-1} K^{-1}, respectively). Figure 4c is shown to isolate the effect of the cooled stage, since the film was also deposited using 75% N_2. With grain sizes of roughly 70 nm, this film is also the most thermally conductive reported in this work (~104 W m^{-1} K^{-1}) and clearly exhibits larger grains than either of the films presented.

Further inspection of the HR-TEM images suggests that the state of the film−substrate interface is a potential driver of transport, as shown in Figure 5. Analysis by a fast Fourier
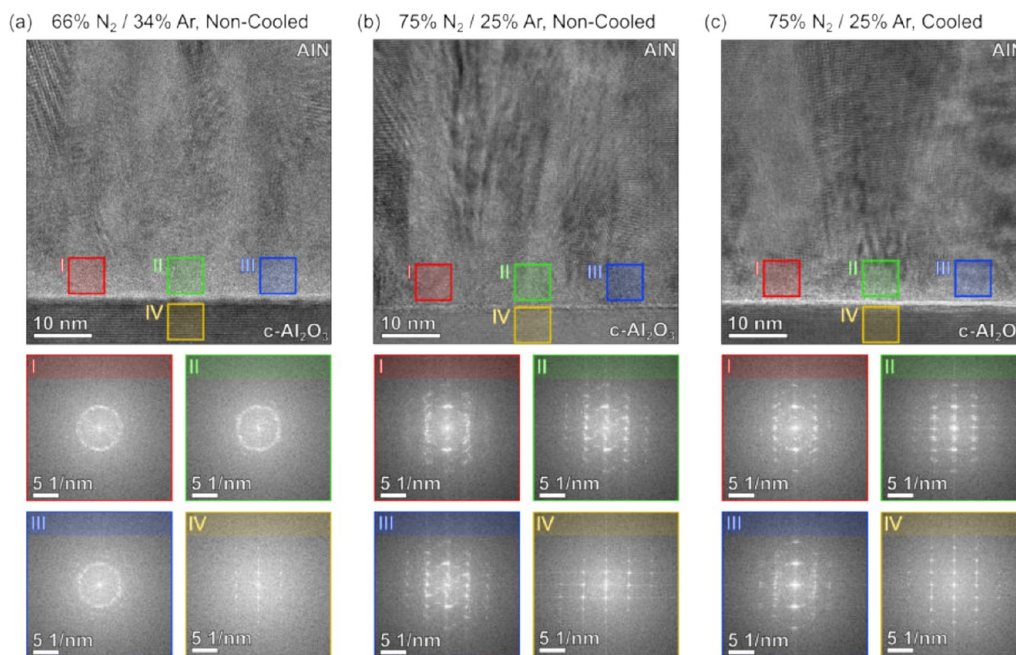
Figure 5. HR-TEM and FFT analysis of film crystallinity at the substrate interface of three key films deposited on c-Al$_2$O$_3$ using different conditions: (a) 66% N$_2$ and 34% Ar on a non-cooled stage, (b) 75% N$_2$ and 25% Ar without stage cooling, and (c) 75% N$_2$ and 25% Ar with the stage cooled to 10 °C throughout deposition.

transform (FFT) is provided for each film in three different near-interface regions (I−III) and for each underlying c-Al$_2$O$_3$ substrate (IV) for comparison. An amorphous layer develops at the AlN/c-Al$_2$O$_3$ interface for the film deposited with 66% N$_2$, further confirmed by the presence of rings rather than discrete diffraction spots in Figure 5a, I−III. This amorphous layer may be the result of an excess of energetic Ar ions bombarding the growth surface during initial deposition, resulting in amorphization at the initial stages of growth, as observed in existing literature reports.[19] This effect is reduced for both films deposited using 75% N$_2$, using the noncooled and cooled stages in Figure 5b,c, respectively. Both of these films exhibit stronger crystallinity above the interface and an "abrupt" character that is more prominent still for the film deposited with a cooled stage. It is likely that the substrate cooling in Figure 5c may have minimized adatom mobility during the initial growth, considering established qualitative models attributing such mobility to larger nucleation sites for crystal growth.[50] However, lower substrate temperatures can also provide a more favorable thermodynamic environment for the formation of nuclei, thereby leading to the formation of more uniformly sized and evenly distributed crystallites. Coupled with suspected reduced strain due to higher quality interfaces, both effects can lead to a more relaxed crystal lattice structure upon cooling, resulting in fewer defects and a more ordered crystal structure.[54−56] In practice, these effects are most easily observed in the larger and more uniformly sized crystallite columns in Figure 4c as compared with Figure 4b.

Thermal boundary conductance measurements of the AlN/substrate interface reaffirm our microstructural results and lend validity to the most thermally conductive films reported in this work. As shown in Figure 6, the extracted AlN/substrate thermal boundary conductance values are compared with predictions from the diffuse mismatch model (DMM)[57,58] with a Born−von Karman (BVK) phonon dispersion approximation (see Section S8 in the Supporting Information). The DMM
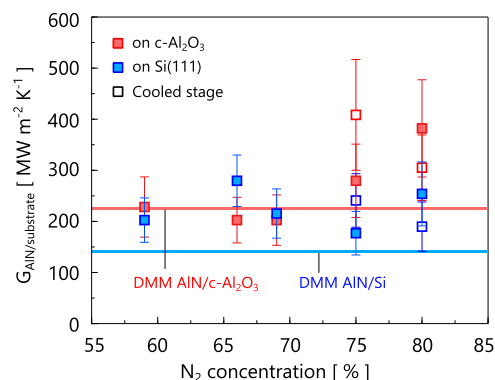

Figure 6. AlN/substrate thermal boundary conductances ($G_{AlN/substrate}$) determined for our AlN films deposited on both Si(111) and c-Al$_2$O$_3$. We note the increasing trend of the AlN/ubstrate thermal boundary conductance upon stage cooling, suggesting the creation of a more well-matched interface, further reinforced with the TEM analysis in Figure 5. All data are from the present study.

thermal boundary conductance (G_{DMM}) from material A to B is given by

$$G_{A \rightarrow B} = \frac{1}{4} \sum_j \int_0^\infty v_{A,j} \hbar \omega D_A(\omega) \frac{\partial f_{BE}^0(\omega, T)}{\partial T} \alpha_{A \rightarrow B} \, d\omega$$

(1)

where j is the phonon branch, v is the phonon velocity in material A, $D_A(\omega)$ is the phonon density of states in material A at phonon frequency ω, f_{BE}^0 is the Bose−Einstein equilibrium function, and $\alpha_{A \rightarrow B}$ is the transmissivity from material A to B. Despite the DMM's inability to capture atomic-scale interface characteristics,[59] it is in broad agreement with our measured values for samples deposited with a noncooled stage, ranging from ∼170 to ∼280 MW m^{-2} K^{-1}. However, the general effect
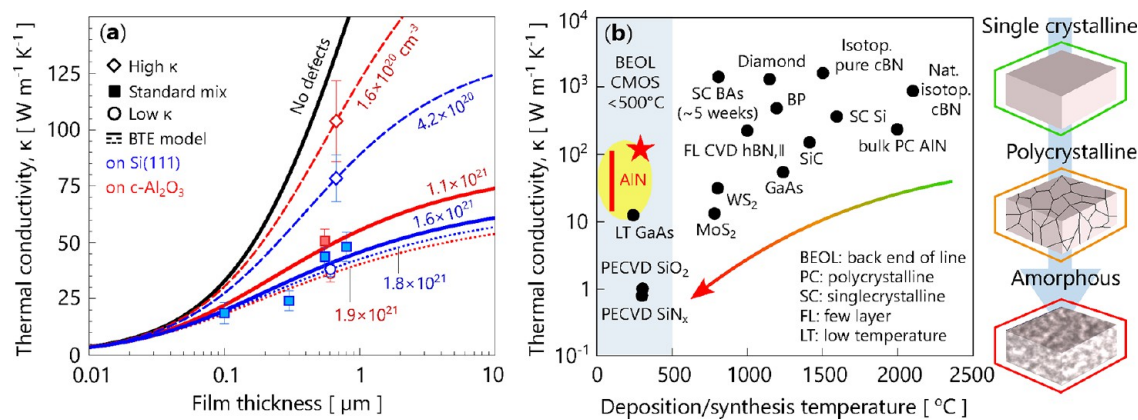
Figure 7. Thermal conductivity with respect to (a) the film thickness for samples in this study and (b) the deposition or synthesis temperature. In (a), the lines correspond to BTE predictions of eq 2 by fitting a defect density to the experimental data, revealing a modulation of roughly 1 order of magnitude. Here, high and low κ refer to the highest and lowest thermal conductivity films reported in this work. (b) Plot of thermal conductivity as a function of deposition temperature demonstrating the appeal for BEOL-compatible deposition of AlN films with high thermal conductivity relative to other materials commonly used in electronic devices.[16,43,65−74]

of a cooled stage is to increase the AlN/substrate thermal boundary conductance, as shown by the open symbols in Figure 6. This increase is more notable for AlN on c-Al₂O₃, which is also the substrate that produced our most thermally conductive film, attributed to more favorable lattice matching compared to Si(111). Indeed, stage cooling also increased the AlN/substrate thermal boundary conductance of films deposited with Kr gas in place of Ar, thus reinforcing this trend. Though large uncertainties prevent a more decisive conclusion due to suppressed sensitivities typical of embedded interfaces, the sharp increase of thermal boundary conductances is evident. This is important from a device perspective, where high-quality interfaces not only promote crystalline growth but can also dissipate more thermal energy to mitigate high operating temperatures and hot spots.[31] A summary of all conductance values is provided in Section S9 in the Supporting Information.

The underlying phonon scattering mechanisms in these AlN films were analyzed with an analytical model based on the Boltzmann transport equation (BTE). We employed a treatment of the BTE in a paradigm similar to past works[16,60−62]

$$\kappa = \frac{1}{3}Cv\lambda = \frac{1}{3}\sum_j \int_0^{\omega_{max}} \hbar\omega D(\omega) \frac{\partial f_{BE}^0(\omega, T)}{\partial T} v_j^2 \tau_j(\omega)\, d\omega$$

(2)

where C is the volumetric heat capacity, λ is the phonon mean free path, ω_{max} is the Debye cutoff frequency, and $\tau(\omega)$ is the phonon relaxation time. Umklapp, defect, and boundary scattering comprise the relaxation time and are summed in accordance with Matthiessen's rule (see Section S10 in the Supporting Information). Specifically, the point defect scattering rate can be expressed as[63]

$$\frac{1}{\tau_D} = \frac{V}{4\pi v^3}\omega^4 \sum_i f_i \left(\frac{m - m_i}{m}\right)^2$$

(3)

where f_i is the fractional concentration of the ith impurity atom and m and m_i are the masses of the original and ith impurity atoms, respectively. We make an important simplification in light of previous studies[16,64] that suggest Al vacancies play a dominant role due to the large atomic mass difference between

Al and common impurities (e.g., Si, O, C, and N atoms). As such, the Al defect density is used as a fitting parameter in conjunction with our experimental data.

The foregoing BTE model sheds light on the degree of defect modulation occurring in our AlN films, as shown in Figure 7a. Here, a solid black line is provided to indicate the model behavior in the limit of no defects, and a fit of the model to the thickness-dependent experimental data using the standard 75% N₂ composition is also shown for comparison. We note that the defect-free thermal conductivity of ~600 nm thick AlN is ~150 W m⁻¹ K⁻¹, suggesting that we reached up to 66% of this limit in the present work, even with films deposited at sub-100 °C temperature. In addition, changing the sputter gas composition alters the defect densities in the present films by over an order of magnitude, from 1.6×10^{20} to 1.9×10^{21} cm⁻³. Such values are in agreement with similar predictions for AlN films, although even the purest films still possess a defect density an order of magnitude greater than that of the bulk.[16] Clearly, Al vacancies play a role in transport that is further elucidated by complementary electrical measurements detailed in Section S11 in the Supporting Information. Our electrical breakdown tests point to a larger relative dielectric constant in the 11.5−11.9 range for our standard 75% N₂ composition (the relative dielectric constant[34] of bulk AlN is ~9.2). Following measurements with Auger electron spectroscopy (Section S4 in the Supporting Information), the AlN films exhibit Al-rich compositions, which are suspected to increase the polarization character of AlN and the accompanying dielectric constant. This is in contrast to Al vacancies, which tend to decrease the dielectric constant. Although more rigorous characterization is needed to deduce the exact impurities present, these results nonetheless provide an intricate set of thermal interface and intrinsic thermal conductivity properties that can be tuned to a great degree.

Finally, Figure 7b provides a landscape of other materials used in electronic devices with respect to deposition temperature.[16,43,65−74] There is broadly a positive correlation between the thermal conductivity and deposition temperature in all the materials shown that is emphasized by the multicolored arrow. In this context, materials exhibiting both high thermal conductivity and electrical resistivity deposited at

low temperatures are desirable. Our results substantiate the modulation of thermal conductivity via a structure−processing−property relationship while maintaining <500 °C BEOL temperatures using WBG materials and are thus attractive candidates for integration in electronic applications requiring high operating frequencies and the handling of high power density.[3,5]

CONCLUSION

We studied sputter-deposited AlN films between 100 nm and 1.7 μm thicknesses, revealing the highest thermal conductivity reported to date in ∼600 nm films with low deposition temperature (<100 °C). At the ∼600 nm thickness, we also observed an ∼3× change in thermal conductivity by controlling the sputtering gas composition during deposition. We elucidated these effects via direct characterization by XRD, TEM, and HR-TEM, which complemented thermal conductivity measurements by TDTR. Analytical models of thermal conductivity based on the Boltzmann transport equation reveal estimated defect densities varying over an order of magnitude, between 1.6×10^{20} and 1.9×10^{21} cm^{-3}. The highest thermal conductivity values are found for depositions onto a cooled stage, which improved the film morphology. Across the entire sample set, correlations between thermal conductivity and microstructure confirm the importance of grain size and the quality and uniformity of the interfacial crystallinity, which are further reinforced by measurements of the thermal boundary conductance. Overall, these results show the potential of AlN as a heat-spreading material with low-temperature BEOL-compatible deposition parameters that can offer application-specific strategic heat spreading or thermal confinement.

MATERIALS AND METHODS

AlN Film Deposition. Sputtered AlN films were deposited using 100 W DC power on a 2 in. Al target after a standard target cleaning and conditioning procedure. All substrates were degreased with a series of solvent rinses. Si substrates were cleaned using a cyclic 2% HF etch, and c-Al$_2$O$_3$ substrates were cleaned by soaking in a 3:1 sulfuric acid and phosphoric acid mixture. More detailed descriptions of these procedures can be found in Section S1 in the Supporting Information.

Diffraction, Ellipsometry, and Transmission Electron Microscopy. Following deposition of the AlN films, all samples were analyzed by Bragg−Brentano X-ray diffraction (XRD) to assess their crystallinity. Grain sizes were estimated by the Debye−Scherrer formula based on AlN (002) diffraction peak full-width at half-maximum (FWHM) fits determined using Rigaku GlobalFit software, as described in Section S3 in the Supporting Information. The thickness of the sputtered films was measured using a J.A. Woollam M-2000D spectroscopic ellipsometer at 75° incidence angle across 500 wavelengths from 190 to 1000 nm. Lamellae from select samples on c-sapphire substrates were prepared using a focused ion beam system with final thinning to ∼35 nm by Eurofins EAG Laboratories (Sunnyvale, CA). Transmission electron microscopy (TEM) and high-resolution TEM (HR-TEM) was performed using a Thermo-Fisher Talos F200X G2 instrument equipped with a 4k × 4k Ceta CMOS camera and double-tilt sample holder. All image processing and fast Fourier transform (FFT) analysis were performed using the Gatan Microscopy Suite.

Raman and Auger Spectroscopy. The highest and lowest thermal conductivity AlN films on both Si(111) and c-Al$_2$O$_3$ substrates were analyzed using Raman spectroscopy (Horiba Labram HR Evolution). Depth-profiling Auger spectroscopy was carried out using a 10 kV (10 nA) electron beam with samples deposited on Si(111) to avoid charging. Two measurements were collected before

sputtering, and then additional measurements were collected after sputtering in 1 min increments to remove surface contamination and prevent carbon buildup, as described and plotted in Section S4 in the Supporting Information.

Time-Domain Thermoreflectance. The thermal conductivity of the AlN films was measured with time-domain thermoreflectance (TDTR), an optical pump−probe method used extensively to determine the thermal properties of nanoscopic materials.[30−32] Knife-edge measurements of the focused spot sizes provided $1/e^2$ beam radii of 5.36 ± 0.1 and 3.19 ± 0.05 for the pump and probe, respectively. Additionally, a pump modulation frequency of 10 MHz and total emitted power of 12.5 mW were applied. The reported mean values are determined from multiple measurements across the samples on different days, while the error bars represent one standard uncertainty determined from the standard deviations of the fitted values, uncertainties in the assumed parameters, and residuals between the model and data. Sensitivity analysis, calibration data, and additional thermal boundary conductance data are included in Section S6 and S9 in the Supporting Information.

ASSOCIATED CONTENT

Ⓢ Supporting Information

The Supporting Information is available free of charge at https://pubs.acs.org/doi/10.1021/acsnano.3c05485.

> Detailed descriptions and figures of the sputter deposition, X-ray diffraction analysis, Raman and Auger analysis, time-domain thermoreflectance (TDTR) measurements, TDTR sensitivity and uncertainty analyses, summary of all thermal boundary conductance values, the Boltzmann transport model used in this work, and secondary electrical breakdown tests (PDF)

AUTHOR INFORMATION

Corresponding Authors

Christopher Perez − *Department of Mechanical Engineering, Stanford University, Stanford, California 94305, United States; Materials Physics, Sandia National Laboratories, Livermore, California 94550, United States;* ⓞ orcid.org/0000-0002-9628-2027; Email: cprez@alumni.stanford.edu

Suhas Kumar − *Materials Physics, Sandia National Laboratories, Livermore, California 94550, United States;* Email: su1@alumni.stanford.edu

Kenneth E. Goodson − *Department of Mechanical Engineering and Department of Materials Science and Engineering, Stanford University, Stanford, California 94305, United States;* Email: goodson@stanford.edu

Authors

Aaron J. McLeod − *Department of Chemistry and Biochemistry, University of California San Diego, La Jolla, California 92093, United States;* ⓞ orcid.org/0000-0002-3720-0992

Michelle E. Chen − *Department of Materials Science and Engineering, Stanford University, Stanford, California 94305, United States*

Su-in Yi − *Department of Electrical and Computer Engineering, Texas A&M University, College Station, Texas 77843, United States*

Sam Vaziri − *Taiwan Semiconductor Manufacturing Company, San Jose, California 95134, United States*

Ryan Hood − *Materials Physics, Sandia National Laboratories, Livermore, California 94550, United States*

Scott T. Ueda − *Materials Science and Engineering Program, University of California San Diego, La Jolla, California 92093, United States*

Xinyu Bao − *Taiwan Semiconductor Manufacturing Company, San Jose, California 95134, United States*

Mehdi Asheghi − *Department of Mechanical Engineering, Stanford University, Stanford, California 94305, United States*

Woosung Park − *Division of Mechanical Systems Engineering, Sookmyung Women's University, Seoul 04310, South Korea*

A. Alec Talin − *Materials Physics, Sandia National Laboratories, Livermore, California 94550, United States;* ⓞ orcid.org/0000-0002-1102-680X

Eric Pop − *Department of Electrical Engineering and Department of Materials Science and Engineering, Stanford University, Stanford, California 94305, United States;* ⓞ orcid.org/0000-0003-0436-8534

Andrew C. Kummel − *Department of Chemistry and Biochemistry, University of California San Diego, La Jolla, California 92093, United States;* ⓞ orcid.org/0000-0001-8301-9855

Complete contact information is available at:
https://pubs.acs.org/10.1021/acsnano.3c05485

Notes
The authors declare no competing financial interest.

REFERENCES

(1) Pop, E. Energy dissipation and transport in nanoscale devices. *Nano Research* **2010**, *3*, 147−169.

(2) Pop, E.; Varshney, V.; Roy, A. K. Thermal properties of graphene: Fundamentals and applications. *MRS Bulletin* **2012**, *37*, 1273−1281.

(3) Fu, Y.; et al. Graphene related materials for thermal management. *2D Materials* **2020**, *7*, 012001.

(4) Köroğlu, Ç.; Pop, E. High Thermal Conductivity Insulators for Thermal Management in 3D Integrated Circuits. *IEEE Electron Device Lett.* **2023**, *44* (3), 496−499.

(5) Oh, S. K.; Lundh, J. S.; Shervin, S.; Chatterjee, B.; Lee, D. K.; Choi, S.; Kwak, J. S.; Ryou, J.-H. Thermal Management and Characterization of High-Power Wide-Bandgap Semiconductor Electronic and Photonic Devices in Automotive Applications. *Journal of Electronic Packaging* **2019**, *141* (2), 020801.

(6) Xu, J.; Yin, W.-y.; Member, S.; Mao, J.; Member, S. Transient Thermal Analysis of GaN Heterojunction Transistors (HFETs) for High-Power Applications. *IEEE Microwave and Wireless Components Letters* **2007**, *17*, 55−57.

(7) Meneghesso, G.; Member, S.; Verzellesi, G.; Danesin, F.; Rampazzo, F.; Zanon, F.; Tazzoli, A.; Member, S.; Meneghini, M.; Member, S.; Zanoni, E.; Member, S.; et al. Reliability of GaN High-Electron-Mobility Transistors: State of the Art and Perspectives. *IEEE Transactions on Device and Materials Reliability* **2008**, *8*, 332−343.

(8) Wyrwas, E.; Condra, L.; Hava, A. Accurate Quantitative Physics-of-Failure Approach to Integrated Circuit Reliability. *IPC APEX EXPO Technical Conference*, 2011; 3:1776, 1815.

(9) Wehmeyer, G.; Yabuki, T.; Monachon, C.; Wu, J.; Dames, C. Thermal diodes, regulators, and switches: Physical mechanisms and potential applications. *Applied Physics Reviews* **2017**, *4*, 041304.

(10) Sood, A.; Xiong, F.; Chen, S.; Wang, H.; Selli, D.; Zhang, J.; Mcclellan, C. J.; Sun, J.; Donadio, D.; Cui, Y.; Pop, E.; Goodson, K. E. An electrochemical thermal transistor. *Nature Communications* **2018**, *9*, 41866−41874.

(11) Chen, M. E.; Rojo, M. M.; Lian, F.; Koeln, J.; Sood, A.; Bohaichuk, S. M.; Neumann, C. M.; Garrow, S. G.; Goodson, K. E.; Alleyne, A. G.; Pop, E. Graphene-based electromechanical thermal switches. *2D Materials* **2021**, *8*, 035055.

(12) Li, J.; Nam, K.; Nakarmi, M.; Lin, J.; Jiang, H.; et al. Band structure and fundamental optical transitions in wurtzite AlN. *Appl. Phys. Lett.* **2003**, *83*, 5163−5165.

(13) Feneberg, M.; Leute, R. A. R.; Neuschl, B.; Thonke, K.; Bickermann, M. High-excitation and high-resolution photoluminescence spectra of bulk AlN. *Physical Review B* **2010**, *82*, 075208.

(14) Albrecht, J. D.; Chang, T.-h.; Kane, A. S.; Rosker, M. J.; Allen, B.; Drive, N. F., *DARPA's Nitride Electronic NeXt Generation Technology Program*. 2010, IEEE Compound Semiconductor Integrated Circuit Symposium (CSICS), Monterey, CA, USA, 2010.

(15) La Spina, L.; Iborra, E.; Schellevis, H.; Clement, M.; Olivares, J.; Nanver, L. Aluminum nitride for heatspreading in RF IC's. *Solid-State Electron.* **2008**, *52*, 1359−1363. Papers Selected from the 37th European Solid-State Device Research Conference - ESSDERC'07.

(16) Xu, R. L.; Rojo, M. M.; Islam, S.; Sood, A.; Vareskic, B.; Katre, A.; Mingo, N.; Goodson, K. E.; Xing, H. G.; Jena, D.; Pop, E. Thermal conductivity of crystalline AlN and the influence of atomic-scale defects Thermal conductivity of crystalline AlN and the influence of atomic-scale defects. *J. Appl. Phys.* **2019**, *126*, 185105.

(17) He, Z.; Yan, Y.; Zhang, Z. Thermal management and temperature uniformity enhancement of electronic devices by micro heat sinks: A review. *Energy* **2021**, *216*, 119223.

(18) Cheng, Z.; et al. Experimental observation of high intrinsic thermal conductivity of AlN. *Physical Review Materials* **2020**, *4*, 044602.

(19) Kuo, P.; Auner, G.; Wu, Z. Microstructure and thermal conductivity of epitaxial AlN thin films. *Thin Solid Films* **1994**, *253*, 223−227.

(20) Koh, Y. R.; et al. Bulk-like Intrinsic Phonon Thermal Conductivity of Micrometer- Thick AlN Films. *ACS Applied Materials & Interfaces* **2020**, *12*, 29443−29450.

(21) Hoque, M. S. B.; et al. High In-Plane Thermal Conductivity of Aluminum Nitride Thin Films. *ACS Nano* **2021**, *15*, 9588−9599.

(22) Deprat, F.; Fenouillet-Beranger, C.; Jousseaume, V.; Guerin, C.; Beugin, V.; Rochat, N.; Licitra, C.; Caubet-Hilloutou, V.; Benoit, D.; Imbert, G.; Rambal, N.; Batude, P.; Vinet, M. Dielectrics stability for intermediate BEOL in 3D sequential integration. *Microelectron. Eng.*

2017, *167*, 90−94. Materials for Advanced Metallization 2016 (MAM 2016).

(23) Fenouillet-Beranger, C. et al. Guidelines for intermediate back end of line (BEOL) for 3D sequential integration. *2017 47th European Solid-State Device Research Conference (ESSDERC)*, 2017; pp 252−255.

(24) Schmitz, J. Low temperature thin films for next-generation microelectronics (invited). *Surf. Coat. Technol.* **2018**, *343*, 83−88. Selected papers of the "E-MRS 2017 − Symposium Q"

(25) Mion, C.; Muth, J. F.; Preble, E. A.; et al. Accurate dependence of gallium nitride thermal conductivity on dislocation density. *Appl. Phys. Lett.* **2006**, *89*, 092123.

(26) Beechem, T. E.; Mcdonald, A. E.; Fuller, E. J.; et al. Size dictated thermal conductivity of GaN Size dictated thermal conductivity of GaN. *J. Appl. Phys.* **2016**, *120*, 095104.

(27) Ueda, S. T.; McLeod, A.; Chen, M.; Perez, C.; Pop, E.; Alvarez, D.; Kummel, A. C. Deposition of High Thermal Conductivity AlN Heat Spreader Films. *2020 International Symposium on VLSI Technology, Systems and Applications, VLSI-TSA 2020* 2020; pp 110−111.

(28) McLeod, A. J.; Ueda, S. T.; Lee, P. C.; Spiegelman, J.; Kanjolia, R.; Moinpour, M.; Woodruff, J.; Kummel, A. C. Pulsed chemical vapor deposition for crystalline aluminum nitride thin films and buffer layers on silicon and silicon carbide. *Thin Solid Films* **2023**, *768*, 139717.

(29) Yalon, E.; Aslan, B.; Smithe, K. K. H.; McClellan, C. J.; Suryavanshi, S. V.; Xiong, F.; Sood, A.; Neumann, C. M.; Xu, X.; Goodson, K. E.; Heinz, T. F.; Pop, E. Temperature-Dependent Thermal Boundary Conductance of Monolayer MoS2 by Raman Thermometry. *ACS Applied Materials and Interfaces* **2017**, *9*, 43013−43020.

(30) Kwon, H.; Perez, C.; Park, W.; Asheghi, M.; Goodson, K. E. Thermal Characterization of Metal−Oxide Interfaces Using Time-Domain Thermoreflectance with Nanograting Transducers. *ACS Applied Materials Interfaces* **2021**, *13*, 58059−58065.

(31) Kwon, H.; Perez, C.; Kim, H. K.; Asheghi, M.; Park, W.; Goodson, K. E. Thermal Interface Enhancement via Inclusion of an Adhesive Layer Using Plasma-Enhanced Atomic Layer Deposition. *ACS Applied Materials and Interfaces* **2021**, *13*, 21905−21913.

(32) Perez, C.; Jog, A.; Kwon, H.; Gall, D.; Asheghi, M.; Kumar, S.; Park, W.; Goodson, K. E. Dominant Energy Carrier Transitions and Thermal Anisotropy in Epitaxial Iridium Thin Films. *Advanced Functional Materials* **2022**, *32*, 2207781.

(33) Jiang, P.; Qian, X.; Yang, R. Time-domain thermoreflectance (TDTR) measurements of anisotropic thermal conductivity using a variable spot size approach. *Rev. Sci. Instrum.* **2017**, *88*, 074901.

(34) Gaskins, J. T.; et al. Review—Investigation and Review of the Thermal, Mechanical, Electrical, Optical, and Structural Properties of Atomic Layer Deposited High- k Dielectrics: Beryllium Oxide, Aluminum Oxide, Hafnium Oxide, and Aluminum Nitride. *ECS Journal of Solid State Science and Technology* **2017**, *6*, N189−N208.

(35) Perez, C.; Knepper, R.; Marquez, M. P.; Forrest, E. C.; Tappan, A. S.; Asheghi, M.; Goodson, K. E.; Ziade, E. O. Non-Contact Mass Density and Thermal Conductivity Measurements of Organic Thin Films Using Frequency − Domain Thermoreflectance. *Advanced Materials Interfaces* **2021**, *9*, 2101404.

(36) Zhao, Y.; Zhu, C.; Wang, S.; Tian, J. Z.; Yang, D. J.; Chen, C. K.; Cheng, H.; Hing, P. Pulsed photothermal reflectance measurement of the thermal conductivity of sputtered aluminum nitride thin films. *J. Appl. Phys.* **2004**, *96*, 4563−4568.

(37) Choi, S. R.; Kim, D.; Choa, S.-h.; Lee, S.-h.; Kim, J.-k. Thermal Conductivity of AlN and SiC Thin Films. *International Journal of Thermophysics* **2006**, *27*, 896−905.

(38) Duquenne, C.; et al. Thermal conductivity of aluminium nitride thin films prepared by reactive magnetron sputtering. *Journal of Physics D: Applied Physics* **2012**, *45*, 015301.

(39) Pan, T. S.; Zhang, Y.; Huang, J.; Zeng, B.; Hong, D. H.; Wang, S. L.; Zeng, H. Z.; Gao, M.; Huang, W.; Lin, Y. Enhanced thermal conductivity of polycrystalline aluminum nitride thin films by optimizing the interface structure. *J. Appl. Phys.* **2012**, *112*, 044905.

(40) Aissa, K. A.; Semmar, N.; Achour, A.; Simon, Q.; Petit, A.; Camus, J.; Boulmer-Leborgne, C.; Djouadi, M. A. Achieving high thermal conductivity from AlN films deposited by high-power impulse magnetron sputtering. *Journal of Physics D: Applied Physics* **2014**, *47*, 355303.

(41) Bian, Y.; Liu, M.; Ke, G.; Chen, Y.; Dibattista, J.; Chan, E.; Yang, Y. Surface & Coatings Technology Aluminum nitride thin film growth and applications for heat dissipation. *Surface & Coatings Technology* **2015**, *267*, 65−69.

(42) Alvarez-Escalante, G.; Page, R.; Hu, R.; Xing, H. G.; Jena, D.; Tian, Z. High thermal conductivity and ultrahigh thermal boundary conductance of homoepitaxial AlN thin films. *APL Materials* **2022**, *10*, 011115.

(43) Slack, G. A.; Tanzilli, R.; Pohl, R.; Vandersande, J. The intrinsic thermal conductivity of AlN. *J. Phys. Chem. Solids* **1987**, *48*, 641−647.

(44) Rounds, R.; Sarkar, B.; Alden, D.; Guo, Q.; Klump, A.; Hartmann, C.; Nagashima, T.; Kirste, R.; Franke, A.; Bickermann, M.; Kumagai, Y.; Sitar, Z.; Collazo, R. The influence of point defects on the thermal conductivity of AlN crystals. *J. Appl. Phys.* **2018**, *123*, 185107.

(45) Jacquot, A.; Lenoir, B.; Dauscher, A.; Verardi, P.; Craciun, F.; Stolzer, M.; Gartner, M.; Dinescu, M. Optical and thermal characterization of AlN thin films deposited by pulsed laser deposition. *Appl. Surf. Sci.* **2002**, *186*, 507−512.

(46) Belkerk, B. E.; Camus, J.; Garnier, B.; Brithen, H. A.; Sahli, S.; Djouadi, M. A. Measuring anisotropic thermal conductivity of aluminum nitride films with the ultra-fast hot strip technique. *International Journal of Thermal Sciences* **2020**, *151*, 106259.

(47) Hirama, K.; Taniyasu, Y.; Kasu, M. AlGaN/GaN high-electron mobility transistors with low thermal resistance grown on single-crystal diamond (111) substrates by metalorganic vapor-phase epitaxy. *Appl. Phys. Lett.* **2011**, *98*, 162112.

(48) Chen, J.-T.; Pomeroy, J. W.; Rorsman, N.; Xia, C.; Virojanadara, C.; Forsberg, U.; Kuball, M.; Janzén, E. Low thermal resistance of a GaN-on-SiC transistor structure with improved structural properties at the interface. *J. Cryst. Growth* **2015**, *428*, 54−58.

(49) Shinoda, H.; Mutsukura, N. Structural properties of GaN and related alloys grown by radio-frequency magnetron sputter epitaxy. *Thin Solid Films* **2008**, *516*, 2837−2842.

(50) Kumada, T.; Ohtsuka, M.; Fukuyama, H. Influence of substrate temperature on the crystalline quality of AlN layers deposited by RF reactive magnetron sputtering. *AIP Advances* **2015**, *5*, 017136.

(51) Sproul, W.; Christie, D.; Carter, D. Control of reactive sputtering processes. *Thin Solid Films* **2005**, *491*, 1−17.

(52) Cho, J.; Francis, D.; Chao, P. C.; Asheghi, M.; Goodson, K. E. Cross-Plane Phonon Conduction in Polycrystalline Silicon Films. *Journal of Heat Transfer* **2015**, *137*, 071303.

(53) Matsunami, N.; Kakiuchida, H.; Sataka, M.; Okayasu, S. XRD Characterization of AlN Thin Films Prepared by Reactive RF-Sputter Deposition. *Advances in Materials Physics and Chemistry* **2013**, *03*, 101−107.

(54) El Akkad, F.; Marafi, M.; Punnoose, A.; Prabu, G. Effect of substrate temperature on the structural, electrical and optical properties of ITO films prepared by RF magnetron sputtering. *Physica Status Solidi (A) Applied Research* **2000**, *177*, 445−452.

(55) Gonçalves, C.; Charvet, S.; Zeinert, A.; Clin, M.; Zellama, K. Nanocrystalline silicon thin films prepared by radiofrequency magnetron sputtering. *Thin Solid Films* **2002**, *403-404*, 91−96.

(56) Jin, H.; Feng, B.; Dong, S.; Zhou, C.; Zhou, J.; Yang, Y.; Ren, T.; Luo, J.; Wang, D. Influence of substrate temperature on structural properties and deposition rate of AlN thin film deposited by reactive magnetron sputtering. *J. Electron. Mater.* **2012**, *41*, 1948−1954.

(57) Little, W. The transport of heat between dissimilar solids at low temperatures. *Canadian Journal of Physics* **1959**, *37*, 334−349.

(58) Swartz, E. T.; Pohl, R. O. Thermal boundary resistance. *Rev. Mod. Phys.* **1989**, *61*, 605−668.

(59) Monachon, C.; Weber, L.; Dames, C. Thermal Boundary Conductance: A Materials Science Perspective. *Annual Review of Materials Research* **2016**, *46*, 433−463.

(60) Liu, W.; Balandin, A. A. Thermal conduction in AlxGa1-xN alloys and thin films. *J. Appl. Phys.* **2005**, *97*, 073710.

(61) Yi, S. I.; Yu, C. Modeling of thermoelectric properties of SiGe alloy nanowires and estimation of the best design parameters for high figure-of-merits. *J. Appl. Phys.* **2015**, *117*, 035105.

(62) Yi, S. I.; Attari, V.; Jeong, M.; Jian, J.; Xue, S.; Wang, H.; Arroyave, R.; Yu, C. Strain-induced suppression of the miscibility gap in nanostructured Mg2Si-Mg2Sn solid solutions. *Journal of Materials Chemistry A* **2018**, *6*, 17559−17570.

(63) Morelli, D. T.; Heremans, J. P.; Slack, G. A. Estimation of the isotope effect on the lattice thermal conductivity of group IV and group III-V semiconductors. *Physical Review B - Condensed Matter and Materials Physics* **2002**, *66*, 1953041−1953049.

(64) Gaddy, B. E.; Bryan, Z.; Bryan, I.; Xie, J.; Dalmau, R.; Moody, B.; Kumagai, Y.; Nagashima, T.; Kubota, Y.; Kinoshita, T.; Koukitu, A.; Kirste, R.; Sitar, Z.; Collazo, R.; Irving, D. L. The role of the carbon-silicon complex in eliminating deep ultraviolet absorption in AlN. *Appl. Phys. Lett.* **2014**, *104*, 202106.

(65) Slack, G. A.; Glassbrenner, C. J. Thermal conductivity of Si and Ge from 3K to the melting point. *Phys. Rev.* **1964**, *134*, A1058−A1069.

(66) Morelli, D. T.; Beetz, C. P.; Perry, T. A. Thermal conductivity of synthetic diamond films. *J. Appl. Phys.* **1988**, *64*, 3063−3066.

(67) Lee, S. M.; Cahill, D. G. Heat transport in thin dielectric films. *J. Appl. Phys.* **1997**, *81*, 2590−2595.

(68) Jackson, A. W.; Ibbetson, J. P.; Gossard, A. C.; Mishra, U. K. Reduced thermal conductivity in low-temperature-grown GaAs. *Appl. Phys. Lett.* **1999**, *74*, 2325−2327.

(69) Ziade, E.; Yang, J.; Brummer, G.; Nothern, D.; Moustakas, T.; Schmidt, A. J. Thickness dependent thermal conductivity of gallium nitride. *Appl. Phys. Lett.* **2017**, *110* (3), 031903.

(70) Yan, R.; Simpson, J. R.; Bertolazzi, S.; Brivio, J.; Watson, M.; Wu, X.; Kis, A.; Luo, T.; Walker, A. R. H.; Xing, H. G. Thermal conductivity of monolayer molybdenum disulfide obtained from temperature-dependent Raman spectroscopy. *ACS Nano* **2014**, *8*, 986−993.

(71) Peimyoo, N.; Shang, J.; Yang, W.; Wang, Y.; Cong, C.; Yu, T. Thermal conductivity determination of suspended mono- and bilayer WS2 by Raman spectroscopy. *Nano Research* **2015**, *8*, 1210−1221.

(72) Lin, Z.; Liu, C.; Chai, Y. High thermally conductive and electrically insulating 2D boron nitride nanosheet for efficient heat dissipation of high-power transistors. *2D Materials* **2016**, *3*, 041009.

(73) Kang, J. S.; Li, M.; Wu, H.; Nguyen, H.; Hu, Y. Experimental observation of high thermal conductivity in boron arsenide. *Science* **2018**, *361*, 575−578.

(74) Chen, K.; et al. Ultrahigh thermal conductivity in isotope-enriched cubic boron nitride. *Science* **2020**, *367*, 555−559.

Supporting Information for High Thermal Conductivity of Sub-Micron Aluminum Nitride Thin Films Sputter-Deposited at Low Temperature

Christopher Perez[1,2*], Aaron McLeod[3], Michelle Chen[4], Su-in Yi[5], Sam Vaziri[6], Ryan Hood[2], Scott T. Ueda[3], Xinyu Bao[6], Mehdi Asheghi[1], Woosung Park[7,8], A. Alec Talin[2], Suhas Kumar[2], Eric Pop[4,9], Andrew Kummel[3], and Kenneth E. Goodson[1,4*]

[1]Department of Mechanical Engineering, Stanford University, Stanford, California 94305, USA
[2]Materials Physics, Sandia National Laboratories, Livermore, CA 94550, USA
[3]Department of Chemistry and Biochemistry, University of California, San Diego, San Diego, USA
[4]Department of Materials Science and Engineering, Stanford University, Stanford, California 94305, USA
[5]Department of Electrical and Computer Engineering, Texas A&M University, College Station, TX 77843, USA
[6]Taiwan Semiconductor Manufacturing Company, San Jose, CA 95134, USA
[7]Division of Mechanical Systems Engineering, Sookmyung Women's University, Seoul, 04310, South Korea
[8]Institute of Advanced Materials and Systems, Sookmyung Women's University, Seoul, 04310, South Korea
[9]Department of Electrical Engineering, Stanford University, Stanford, CA 94305, USA
*goodson@stanford.edu, cprez@alumni.stanford.edu

Contents

S1. Sputter deposition of AlN

The AlN films were deposited in a home-built vacuum chamber system comprised of a load lock and sputtering chamber, each pumped by individual turbomolecular pumps with base pressures 4×10^{-7} Torr and 1×10^{-7} Torr, respectively.

THe Silicon (111) and c-Al_2O_3 substrates were used in this work were prepared by a degrease with acetone, methanol, and water followed by three cycles of an HF etch consisting of submersion in 2% HF for 30 seconds and rinsing with deionized water for 30 seconds. All substrates were dried under N_2. The sapphire substrates were cleaned using the same degrease process followed by a 20 minute etch in a 3:1 bath of sulfuric acid and phosphoric acid held at 80 °C. Following the etch, sapphire substrates were rinsed with deionized water for 15 seconds before drying under N_2. The substrate coupons were then loaded into the load-lock chamber for pump down; substrates were only transferred into the sputter chamber after the load-lock had reached its base pressure.

A 2" Al target (99.999%, Kurt J. Lesker Co.) was attached to the sputter cathode (Torus MagKeeper 2, Kurt J. Lesker Co., balanced magnetron configuration) which was fitted with a pneumatic shutter. The target to substrate distance was approximately 10 cm. The substrates were transferred into the sputtering chamber under 20 sccm of Ar and were placed on a grounded copper stage with integrated water-cooling capability. A thermocouple mounted under the substrate holder allowed for monitoring of stage temperature during deposition. The chamber pressure was brought to 6 mTorr with Ar for a two minute target cleaning at 100 W DC. Following this clean, a ramp to the desired N_2/Ar gas composition at approximately 3 mTorr pressure was performed over approximately two minutes. Select depositions were repeated using Kr in place of Ar. A brief pre-sputter of approximately 30 seconds was performed against the target shutter before beginning reactive sputter deposition using 100 W DC. Growth rates ranged from ∼4-6 nm/min in this configuration.

The Ar, and N_2 gasses were obtained from AirGas (99.99%); Kr was obtained from Praxair all gas flows were controlled by a home-built system of mass flow controllers and were purified by an Entegris GateKeeper mounted just before the gas inlet to remove trace oxygen and water contaminants. Pressures were measured using a capacitance manometer (Kurt J. Lesker Co.) mounted on the body of the sputtering chamber.

In the main text, we mention two sets of AlN films deposited for different pu rposes: the first used a standard gas composition of 25% Ar and 75% N_2 with film thicknesses of 685 nm, 1156 nm, and 1735 nm on both Si(111) and c-Al_2O_3 substrates, and the second being approximately 600 nm in thickness to demonstrate the tunability of the room temperature (RT) thermal conductivity by manipulating the sputtering gas composition. A 80 nm Al film to facilitate thermal measurements by acting as an optothermal transducer was then deposited on top of all the samples via in-situ deposition in the chamber for the first set, and electron beam evaporation (AJA International Inc., ATC-E Series) for the second set. Deposited at a nominal chamber pressure of 9.8×10^{-7} Torr with a 0.5 Å s^{-1} deposition rate, the thickness of the Al films were d etermined v ia s canning electron microscopy (SEM).

S2. AlN films sputtered with Krypton

To lend validity to the observed phenomenon using a cooled stage, three additional sets of ∼600 nm thick films were deposited: one using 76% N_2 and 24% Kr without stage cooling, one using 76% N_2 and 24% Kr with stage cooling, and one using 81% N_2 and 24% Kr without stage cooling. The deposition conditions, thicknesses, thermal conductivity values, AlN (002) diffraction peak full-width at half max (FWHM), and estimated crystallite sizes for these films sputtered are shown in Table S1. Also shown are their analogous depositions using Ar. On both Si(111) and c-Al_2O_3, these films showed thermal conductivity and AlN (002) FWHM values similar to those of the films deposited using Ar with no notable improvements.

S3. X-Ray diffraction analysis

Diffraction signal from the AlN (002) peak was used alongside the Debye-Scherrer equation to estimate crystallite size in the sputtered films, given by

$$C.S. = \frac{0.94\lambda}{\beta cos(\theta)} \tag{1}$$

where C.S. is the estimated crystallite size, λ is the x-ray wavelength, β is the peak FWHM in radians, and θ is the diffraction angle. We note that although this model was originally intended for powders, the estimated

Table S1. A comparison of deposition conditions and properties for sputtered AlN films deposited using Ar and Kr as the sputtering gas. We include films sputtered with Ar that are in close to the Kr sputter gas concentrations for comparison.

Substrate	Cooled?	N$_2$%	Ar%	Kr%	d [nm]	κ [W m^{-1} K^{-1}]	(002) FWHM [$^\circ$]	C.S. [nm]
c-Al$_2$O$_3$		75	25		685	50.6 $\pm$ 3.3	0.168	52.0
c-Al$_2$O$_3$	Y	75	25		670	103.9 $\pm$ 17.9	0.126	69.3
c-Al$_2$O$_3$		80	20		639	74.9 $\pm$ 6.4	0.215	40.6
c-Al$_2$O$_3$		76		24	653	60.5 $\pm$ 5.0	0.205	42.6
c-Al$_2$O$_3$	Y	76		24	647	68.1 $\pm$ 8.6	0.207	42.2
c-Al$_2$O$_3$		81		19	661	64.6 $\pm$ 7.6	0.181	48.3
Si(111)		75	25		685	43.7 $\pm$ 4.2	0.222	39.3
Si(111)	Y	75	25		670	78.5 $\pm$ 10.3	0.168	52.0
Si(111)		80	20		639	79.8 $\pm$ 5.5	0.177	49.3
Si(111)		76		24	653	47.5 $\pm$ 3.9	0.244	35.8
Si(111)	Y	76		24	647	51.1 $\pm$ 5.0	0.260	33.6
Si(111)		81		19	661	44.7 $\pm$ 4.1	0.260	33.6

crystallite sizes, i.e. grain sizes, provided are intended solely for comparative purposes within our datasets. Figure S1 summarizes the grain sizes for our AlN films as a function of film thickness.
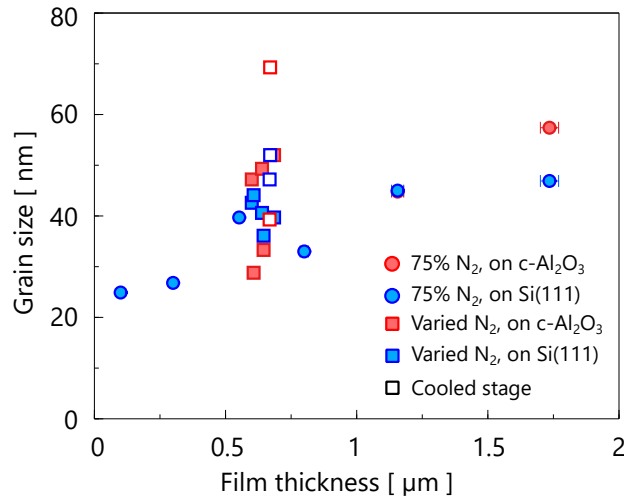

Figure S1. A summary of the calculated grain sizes as a function of film t hickness i n th is w o r k. W e n ote that the grain sizes for the roughly 1 μm film w ere n early i dentical a nd t heir d ata p oints a re a lmost o n t op o f one another.

S4. Raman and Auger spectroscopy

Following the x-ray analyses of the AlN films, samples were analyzed using Raman (Horiba Labram HR Evolution) and depth profiling Auger spectroscopy. For Raman spectrosopy, a 532 nm laser source was used with a grating of 600 l mm^{-1} to optimize signal intensity, measurement range, and spectral resolution. The resulting spectra for both Raman and Auger spectroscopy are shown in Figure S2, with the Raman values listed in Table S2. We show the Raman spectra for the high- and low-thermal conductivity AlN films in Figure S2a and b, respectively, and observe the prototypical E_2(high) peak positions of approximately 655 cm^{-11} emphasized further in Figure S2c and d. We predictably observe smaller FWHM values for more thermally conductive films on Si(111), yet note the opposite trend for films on c-Al$_2$O$_3$. This is surprising given the much larger intensity of the measured signal for the more thermally conductive film, a lbeit w ith m ore n oi se. S ubstrate e ffects fr om this particular sample were attributed to this disparity as its contribution would likely broaden the E_2(high) peaks.

For Auger spectroscopy, measurements were made using a 10 kV (10 nA) electron beam with the highest and lowest thermal conductivity samples deposited on Si(111) to avoid charging. Two measurements were collected
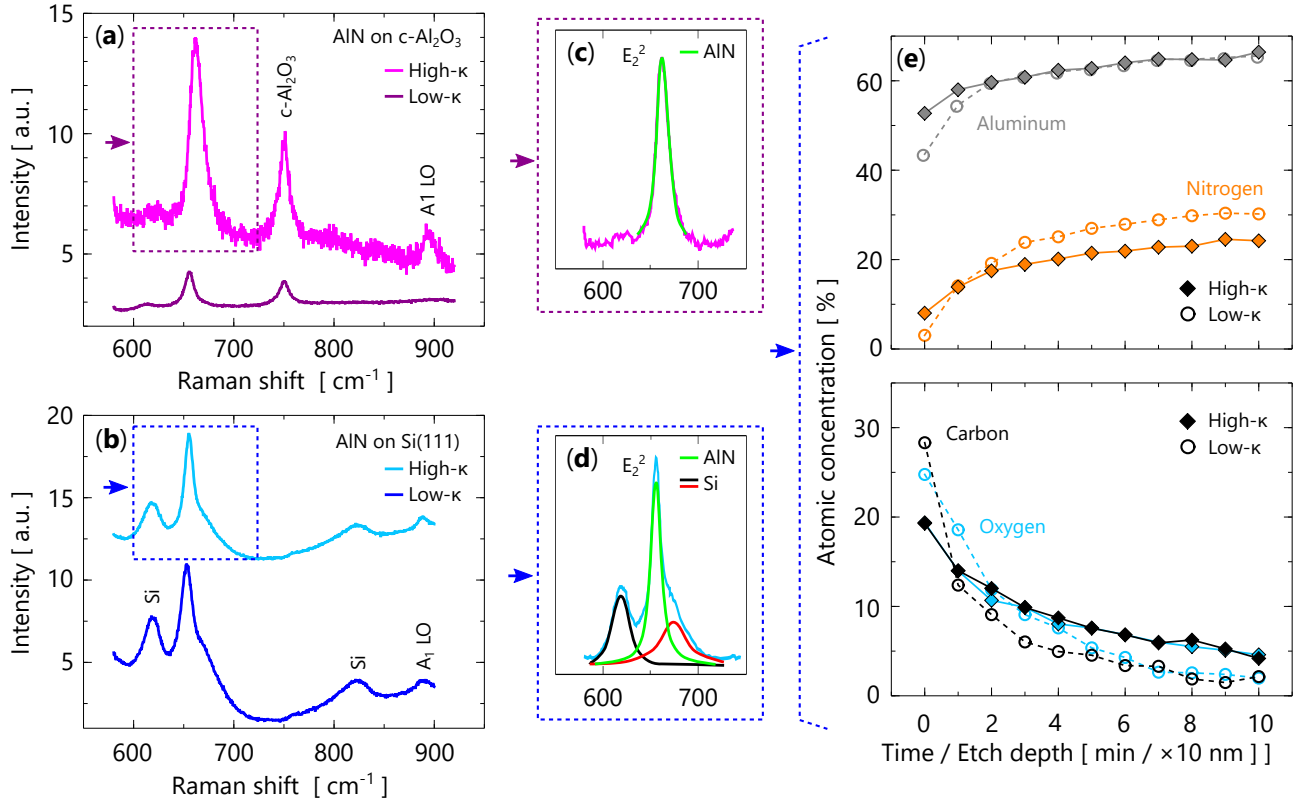
Figure S2. Raman and Auger electron spectroscopy of the highest thermal conductivity [κ] AlN films in this study deposited on (a) c-Al$_2$O$_3$ and (b) Si(111) substrates. Peak fits of the Raman data are shown for AlN films on (c) c-Al$_2$O$_3$ and (d) Si(111), exhibiting FWHM values of 16.8 and 11.6 cm^{-1}, respectively. (e) The chemical composition of the AlN film on Si(111) as a function of etch depth measured with Auger electron spectroscopy.

Table S2. A summary of the E_2 (high) and FWHM values obtained with Raman spectroscopy for the highest and lowest cross-plane thermal conductivity ($\kappa_\perp$) films on both Si(111) and c-Al$_2$O$_3$.

Substrate	$\kappa_\perp$ [W m^{-1} K^{-1}]	E_2 (high) [cm^{-1}]	FWHM [cm^{-1}]
Si(111)	79.8 ± 5.5	655	11.6
Si(111)	38.1 ± 3.2	653	16.0
c-Al$_2$O$_3$	103.9 ± 17.9	663	16.8
c-Al$_2$O$_3$	36.1 ± 3.8	656	11.0

before sputtering, then additional measurements were collected after sputtering in 1 minute increments to remove surface contamination and prevent carbon build-up. Sputtering was performed using a 2 kV, 1 μA Ar ion beam. The sputter rate was calculated to be 10 nm min^{-1} for pure Al at a pressure in the low 10^{-8} Torr range (low 10^{-10} Torr base pressure). We demonstrate the Al,N, C, and O atomic concentrations in Figure S2e, where we observe a high AlN:N stoichiometry that is not 1:1. It is important to note that we do not rely on the Auger data to determine stoichiometry quantitatively, but rather use it as a way to compare the relative contribution of constituent atoms. In this context, the Al-rich nature of our films comes to light, as well as the higher presence of C over O impurities. Such impurities are common with sputter deposition of AlN films, and the usual steps to remove these impurities (e.g. thermal annealing, ultra-high vacuum, etc.) are typically not BEOL-compatible.

S5. Time-domain thermoreflectance (TDTR)

The thermal properties for our AlN films were determined with Time-domain Thermoreflectance (TDTR), as described in the main text. The focused radii of the beams were determined through knife-edge measurements and measured to be 5.36 ± 0.1 and 3.19 ± 0.05 for the pump and probe, respectively. A pump power of 9.5 mW was utilized and modulated with a frequency of 10 MHz. The probe, set to 3 mW, was focused concentrically with the pump onto the sample surface using a 20× objective lens. Thermoreflectance data were then fit to the solution of a 3D heat diffusion model for a multi-layer stack of materials and the unknown properties of interest are used as parameters to converge measurement and theory[2,3].

We note that all controlled parameters were obtained from either independent measurements or from the literature. As such, the thermal conductivity of our Al transducer and substrates were independently determined with TDTR. The thickness of the Al transducer was provided by scanning electron microscopy (SEM) using a our reference Si(111) substrate sample to avoid substrate charging. The resulting uncertainties for independent measurements were inputted into our thermal model to produce the total uncertainty of the measurement. The results are listed in Table S3 and shown in Figure S4a.

Table S3. Properties used to determine the cross-plane thermal conductivty ($\kappa_\perp$) and boundary conductances (Gs) of the AlN thin films. The volumetric heat capacities (ρc_p) are taken from the literature and the thermal conductivity of the Al transducer (κ_{Al}) was found from TDTR using companion SiO$_2$ samples during the Al deposition. The thicknesses for AlN and Al were measured with XRD and scanning electron microscopy (SEM), respectively.

| Material	ρc_p [MJ m^{-3} K^{-1}]	$\kappa_\perp$ [W m^{-1} K^{-1}]	$\kappa_\perp / \kappa_\parallel$	Film thickness [nm]
Al	2.44 ± 0.05[4]	151.2 ± 25.0	1	81.1 ± 1.3
AlN	2.68 ± 0.08[5]	$\kappa_{\perp,AlN} \pm \sigma$	1.5	100−1700
Si	1.66 ± 0.09[6]	142.0 ± 12.0	1	1×10^5
c-Al$_2$O$_3$	3.10 ± 0.09[6]	42.5 ± 3.3	1	1×10^5

S6. TDTR sensitivity

The measurable properties in a TDTR measurement critically depend on the sensitivity of the measured signal to said properties when described by a multilayer heat diffusion model. As such, the sensitivity of the measured TDTR signal to an unknown property x is defined as

$$S_x = \frac{\partial ln(MS)}{\partial ln(x)} \tag{2}$$

where MS is the measured signal, the ratio ($-V_{in}/V_{out}$) in this work. As discussed briefly in the main text, sensitivity calculations were performed for AlN thin film system considering both Si(111) and c-Al$_2$O$_3$ substrates. Input properties for these calculation are summarized in Table S3, where we applied prototypical AlN/substrate and Al/AlN thermal boundary conductances of 200 MW m^{-2} K^{-1}[5]. We assumed 20, 40, and 80 W m^{-1} K^{-1} for the 100, 600, and 1700 nm films, respectively. The assumed beam sizes were taken from knife-edge measurements of the focused spot radii, yielding 5.36 and 3.19 for the pump and probe, respectively. The sensitivity analysis is summarized in Figure S3 for our AlN films.
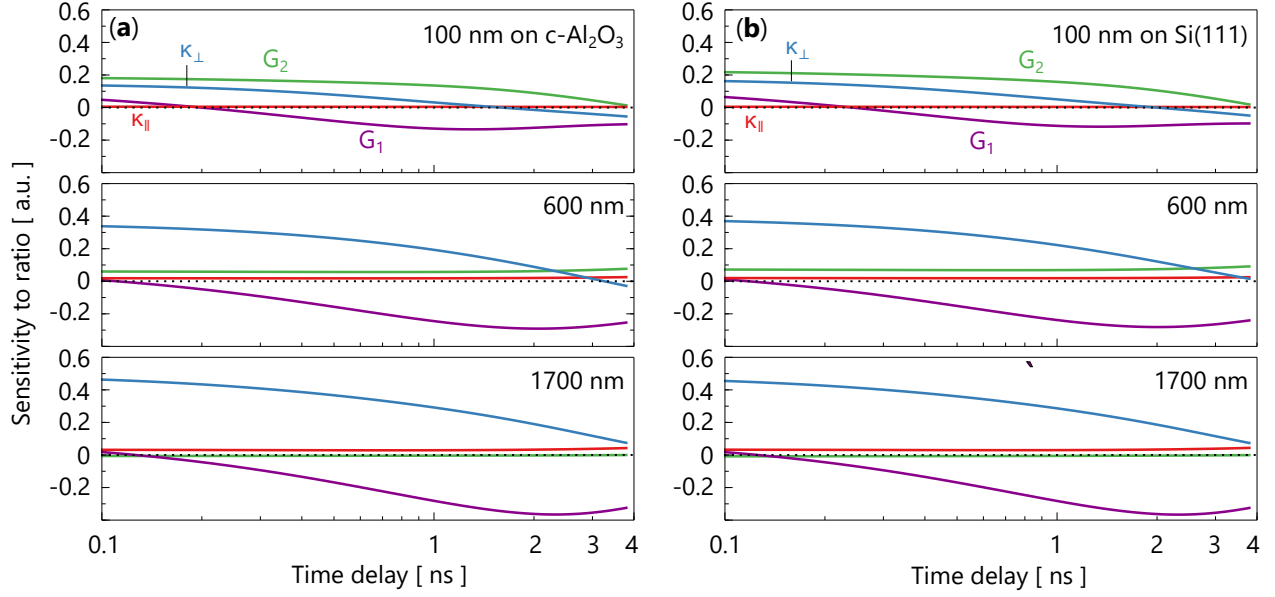
Figure S3. The TDTR measurement sensitivity for the cross- and in-plane thermal conductivity ($\kappa_\perp / \kappa_\parallel$), the Al/AlN thermal boundary conductance (G_1), and the AlN/substrate thermal boundnary conductance (G_2) for AlN films on (a) c -Al$_2$O$_3$ and (b) S i(111). The thicknesses of the films are provided in the insets.

S7. TDTR uncertainty analysis and fitting routine

The standard deviations of the fitted thermal conductivities and thermal boundary conductances for the AlN material systems in this study were calculated based on the variance-covariance matrix $\mathrm{Var}[\widehat{X}_U]$[7]. $\mathrm{Var}[\widehat{X}_U]$ is given by:

$$\mathrm{Var}[\widehat{X}_U] = (J_U^{\star\prime} J_U^\star)^{-1} J_U^{\star\prime} \times (\mathrm{Var}[\Phi] + J_C^\star \mathrm{Var}[X_C] J_C^{\star\prime}) J_U^\star (J_U^{\star\prime} J_U^\star)^{-1} \tag{3}$$

where $J_U^\star$ is the Jacobian matrix with respect to the unknown parameter, $J_C^\star$ is the Jacobian matrix with respect to the controlled parameters (e.g. the thickness of the Al film), $\mathrm{Var}[\Phi]$ is the variance-covariance matrix of the noise of the probe beam, and $\mathrm{Var}[X_C]$ is the variance-covariance matrix of the controlled parameters. We determined $\mathrm{Var}[\Phi]$ by measuring the standard deviation of 40 data points for each measurement trial with the pump beam off. $J_C^\star$ and $\mathrm{Var}[X_C]$ were calculated using the measured values discussed above, and $J_U^\star$ was calculated based on the thermal conductivities and boundary conductances fitted by using the mean controlled parameters and TDTR data.

As mentioned in the main text, we implemented a global optimization approach to provide the greatest measurement fidelity when determining the thermal boundary conductances at the AlN/substrate interfaces. We consider the typical thermal boundary conductance range of semiconductor-dielectric interfaces[5] and determine the uncertainties involved in the Al/AlN thermal boundary conductance, as well as the cross-plane thermal conductivity using Equation 3. Here, normalized uncertainties $\|\sigma\|$ are used

$$\|\sigma\|_x = \frac{\sqrt{\mathrm{Var}[\widehat{X}_U]_x}}{\max\left(\sqrt{\mathrm{Var}[\widehat{X}_U]_x}\right)}, \tag{4}$$

in conjunction with a root-sum-square (RSS) quantity to guide the optimization

$$\mathrm{RSS} = \sqrt{\sum_x \|\sigma\|_x^2}, \tag{5}$$

where x is the property in question for the range of AlN/substrate thermal boundary conductances considered. The cross-plane thermal conductivity and the Al/AlN thermal boundary conductance were fit assuming different values for the range of AlN/substrate thermal boundary conductances since they are the most sensitive properties in our material system. Figure S4b shows example optimizations for our three-parameter fitting using the above expressions and our experimental data for the same AlN film on both c- Al$_2$O$_3$ and Si(111). The uncertainties in our determined thermal boundary conductances were a result of performing such an analysis on several measurement trials of the same sample and noting the shift in the optimized value to define a spot-to-spot variance. The same optimization was then performed using extreme values for each controlled parameter to deduce a conservative variance as a result of the inherent sensitivity to the AlN/substrate parameter. Both these individual contributions were then summed in quadrature to determine a measurement uncertainty.
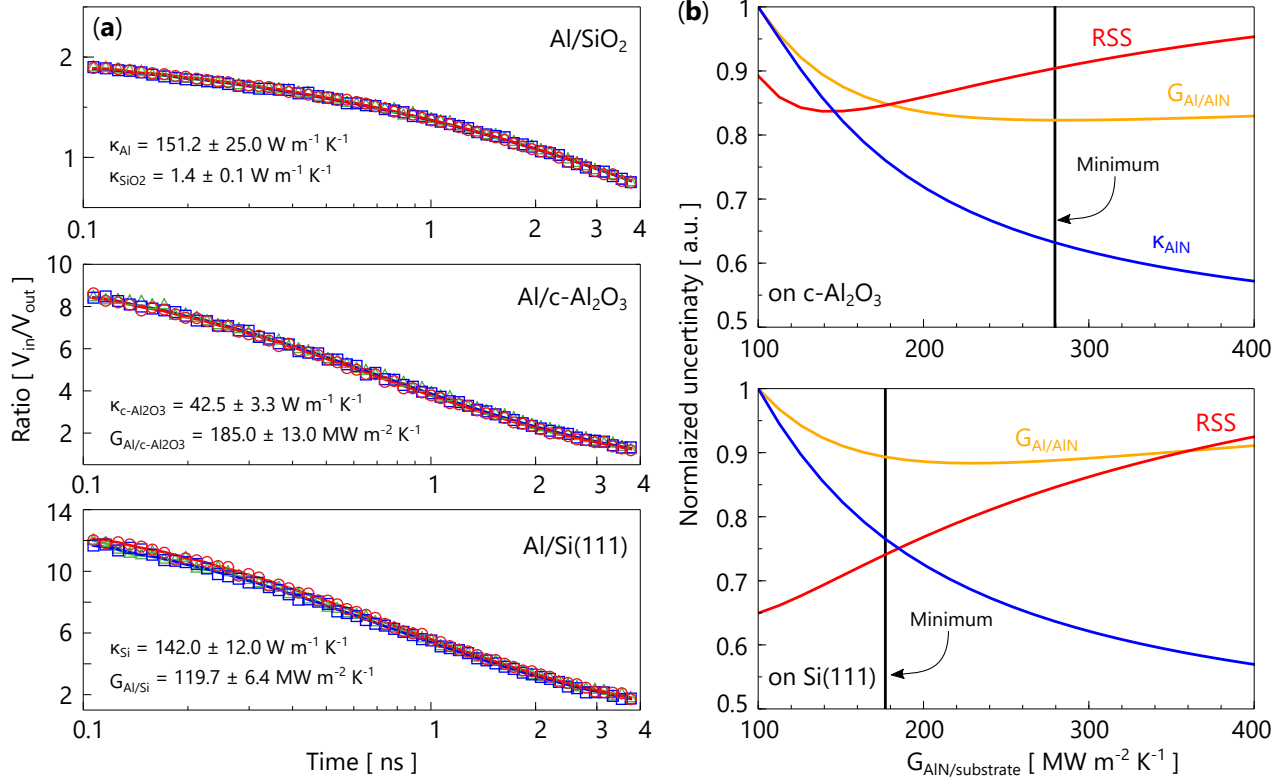
Figure S4. (a) Calibration TDTR measurements for the Al/SiO$_2$, Al/c-Al$_2$O$_3$, and Al/Si(111) material systems used in this work. A companion Al/SiO$_2$ sample was placed in the deposition chamber such that it experienced the same Al deposition as the rest of our samples and was thus used to determine the thermal properties of our Al transducer. (b) Example optimization analysis for our 670 nm thick AlN sample on both c-Al$_2$O$_3$ and Si(111). Using Equation 4 and 5, a minimum in fitting uncertainty was found considering a AlN/substrate thermal boundary conductance range of $100-600$ MW m^{-2} K^{-1}. We note that a range of $100-400$ MW m^{-2} K^{-1} is presented here for clarity.

S8. Thermal boundary conductance predictions

To gain a sense for the changes in the AlN/substrate thermal boundary conductance (G) using our various deposition conditions, we contrast our measurements with predictions from the diffuse mismatch model (DMM)[8, 9] with a Born–von Karman (BVK) phonon dispersion approximation. The DMM thermal boundary conductance (G_{DMM}) from material A to B is given by

$$G_{\mathrm{A}\to\mathrm{B}} = \frac{1}{4}\sum_j \int_0^\infty v_{\mathrm{A},j}\hbar\omega D_{\mathrm{A}}(\omega)\frac{\partial f_{\mathrm{BE}}^0(\omega,T)}{\partial T}\alpha_{\mathrm{A}\to\mathrm{B}}d\omega,$$ (6)

where $\hbar$ is the reduced Planck constant, j is the phonon branch, v_A is the phonon group velocity in material A, $\alpha_{A \rightarrow B}$ is the transmissivity from material A to B, f_{BE}^0 is the Bose-Einstein equilibrium function, and $D_A(\omega)$ is the phonon density of states in material A. We approximate $v_{A,j}$, the phonon velocity in material A for the jth phonon branch, by fitting experimental data[10] for the phonon dispersion relationship obtained in certain symmetry directions by considering interactions of an atom with its neighbors[11].

The resulting thermal boundary conductance values determined with Equation 6 for our AlN/Si(111) and AlN/c-Al$_2$O$_3$ material systems were 140 and 230 MW m^{-2} K^{-1}, respectively. These are in agreement with our determined values for samples deposited with a non-cooled stage, ranging from $\sim$170 to $\sim$280 MW m^{-2} K^{-1}.

S9. Summary of the thermal boundary conductance values

Figure S5 summarizes the thermal boundary conductance values determined in this work. Figure S5a shows the values determined for the 100, 300, and 800 nm AlN films deposited with the standard 75% N$_2$ sputter gas composition on Si(111) substrates. Here, the AlN/Si thermal boundary conductance was found through an optimization of the AlN film cross-plane thermal conductivity and the thermal boundary conductances surrounding the film, since this particular set of films was deposited in the same run. We fixed the AlN/Si thermal boundary conductance since all depositions were identical and such a treatment led to the lowest fitted uncertainties.
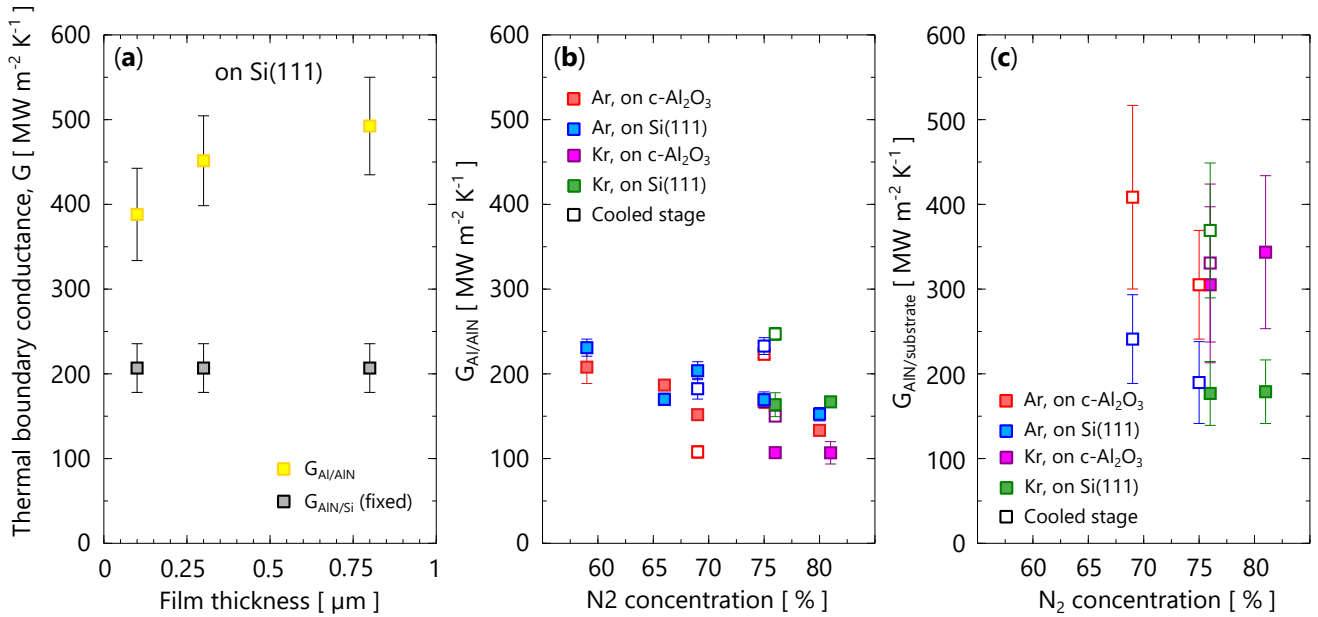
Figure S5. (a) The thermal boundary conductance (G) values determined for the 100, 300, and 800 nm AlN films. These were deposited with the standard 75% N$_2$ sputter gas composition on Si(111) substrates. (b) The Al/AlN thermal boundary conductance values extracted for the $\sim$600 nm films. Also listed are the values for the AlN films deposited with Kr component gas in place of Ar. (c) The AlN/substrate thermal boundary conductances found for the thermally-modulated AlN films in this work. We note that the values for the non-cooled films are not displayed here for clarity, but are provided in Figure 6 of the main text.
)

The exceptionally high thermal boundary conductance values for this set are attributed to the Al transducer deposition being performed in-situ without breaking vacuum. However, these values are still surprising given recent work on Al/GaN interfaces have reported the importance of high temperature depositions and Al deposition under ultra-high vacuum (UHV) for achieving thermal boundary conductances on the order of 500 MW m^{-2} K^{-1}[12]. Indeed, harmonically lattice-matched Al/Al$_2$O$_3$ interfaces with UHV growth conditions yielded smaller values than those reported here, albeit with a different material system[13]. Besides high vacuum conditions, the Al sputtering deposition for this set of films is more energetic than other types (e.g. evaporation)[14] and is also suspected to contribute to a larger Al/AlN thermal boundary conductance.

Figure S5b on the other hand, summarizes the extracted Al/AlN thermal boundary conductance values

extracted for our ~600 nm films. Also listed are the values for the AlN films deposited with Kr component gas in place of Ar. We note a relatively wide variation in the Al/AlN thermal boundary conductances (~100 to ~250 MW m^{-2} K^{-1}), likely due to a convolution between the near-interface crystal structure, surface oxidation, and the surface quality immediately before Al transducer deposition. Although these samples were subjected to a standard solvent clean prior to transducer deposition, surface variation across samples is known to heavily influence the transducer/sample thermal boundary conductance the unless meticulously monitored[14].

The AlN/substrate thermal boundary conductances in our work are shown in Figure S5c. Here, the values for the non-cooled films are not shown for clarity, but are provided in Figure 6 of the main text. As mentioned in the main text, we see a general increase in the AlN/substrate thermal boundary conductance with the implementation of a cooled stage. This is promising since the trend persists when replacing the Ar sputter gas with Kr. HR-TEM of the near-interface region reveals an interface with a more crystalline character and is largely attributed to the increase in thermal boundary conductances and larger cross-plane thermal conductivities.

S10. Boltzmann Transport Equation predictions

As discussed in the main text, we analyze the contributions of different phonons and understand their underlying scattering mechanisms in AlN using an analytical model based on Callaway's model[15] of the Boltzmann transport equation (BTE)[16–19]. The basic BTE modeling of lattice thermal conductivity is expressed as,

$$\kappa = \frac{1}{3}Cv\lambda = \frac{1}{3}\sum_j \int_0^{\omega_{\max}} \hbar\omega D(\omega)\frac{\partial f_{\mathrm{BE}}^0(\omega,T)}{\partial T}v_j^2\tau(\omega)d\omega$$

$$= \sum_j \frac{k_B^4 T^3}{2\pi^2\hbar^3}\left(\frac{1}{v_j}\right)\int_0^{\frac{\theta_{D,j}}{T}}\tau_j\frac{x^4}{(e^x-1)^2}dx, \tag{7}$$

and the Callaway model considers the separate roles of normal scattering (τ_{N}) and other resistive (Umklapp, grain boundary, point defects, etc.) scattering events (τ_p),

$$\kappa = \sum_j \frac{k_B^4 T^3}{2\pi^2\hbar^3}\left(\frac{1}{v_j}\right)\left(I_{1,j}+\frac{I_{2,j}^2}{I_{3,j}}\right), \tag{8}$$

where k_B is the Boltzmann constant, C is the volumetric heat capacity, v is the phonon group velocity, λ is the phonon mean free path, j is the phonon branch which includes two transverse acoustic phonon modes and one longitudinal acoustic mode of AlN, $\omega_{\max}$ is the Debye cutoff frequency, θ_D is the Debye temperature, $D(\omega)$ is the phonon density of states, f_{BE}^0 is the Bose-Einstein equilibrium function, and $\tau(\omega)$ is the phonon relaxation time. The physical processes that comprise the relaxation time are summed in accordance to Matthiessen's rule

$$\frac{1}{\tau_j} = \frac{1}{\tau_{\mathrm{N},j}}+\frac{1}{\tau_{\mathrm{U},j}}+\frac{1}{\tau_{\mathrm{B},j}}+\frac{1}{\tau_{\mathrm{D},j}}, \tag{9}$$

where the subscripts correspond to normal-process (N), Umklapp (U), defect (D), and boundary (B) scattering, respectively. We use an expression for normal processes described by[20]

$$\frac{1}{\tau_{\mathrm{N}}} = \frac{k_B^3\gamma^2 V}{M\hbar^2 v^5}\omega^2 T^3, \tag{10}$$

M is the average mass of an atom in the crystal, and γ is the Grüneisen parameter[21]. V is the unit volume for wurtzite AlN, given by

$$\frac{\sqrt{3}a^2c}{8}, \tag{11}$$

where a and c are lattice parameters, 3.11 and 4.98 Å, respectively[22]. For the Umklapp scattering time, we implemented

$$\frac{1}{\tau_U} = \frac{\hbar\gamma^2}{M\theta_D v^2} e^{-\frac{\theta_D}{3T}} \omega^2 T,$$ (12)

where θ_D is the Debye temperature of 950 K[23]. Boundary scattering is described by[19]

$$\frac{1}{\tau_B} = \frac{d}{v},$$ (13)

where d is the AlN film thickness. Point defect scattering arises from impurity atoms of C, Si, and O, and from Al vacancies. As such, we make use of the following expression[20],

$$\frac{1}{\tau_D} = \frac{V}{4\pi v^3} \omega^4 \sum_i f_i \left(\frac{m - m_i}{m}\right)^2,$$ (14)

where f_i is the fractional concentration of the ith impurity atom, and m and m_i are the masses of original and ith impurity atoms, respectively. As mentioned in the main text, we make important simplification light of previous studies[19] that suggest Al vacancies play a dominant role due to the large atomic mass difference between Al and common impurities (e.g. Si, O, C, and N atoms). Our assumption is further strengthened from prior experimental work that observed how C atoms often substitute for N atoms and Si atoms for Al[24]. Since our model was inspired by that of Xu et al.[19], the results reported here are not expected to differ markedly from a first-principles approach. We do stress, however, that the detailed transport modeling of our AlN films is beyond the scope of this largely experimental and practical work, and we understand that there are more rigorous models (i.e. ab-initio calculations) that can be employed.

S11. Electrical breakdown tests

To assess the electrical characteristics of our AlN films as passivation materials, we performed electrical breakdown tests. AlN deposition was performed on top of a film of a highly doped Si substrate which served as a global back electrode. Rougly 195 μm radius circles ('dots') were patterned using a shadow mask and e-beam evaporation (3 nm Ti/40 nm Au) on top of the AlN film to define the top electrode. We note that the standard 75% N_2 composition was used for these tests (685 nm thick), the results of which are shown in Figure S6.

Each set of colored circles shown represents measurements performed one of 11 metal-insulator-metal structures: we performed both frequency- and voltage-dependent capacitance measurements using a parallel resistor and capacitor model. Our average extracted dielectric constant, however, was similar for both types of experiments and ranged from 11.5-11.9. Also included is the bulk dielectric constant for AlN[5], which is notable smaller than that of our film. Considering the Al-rich nature of our films seen in the Auger analysis in Figure S2(e), Al atoms are expected to increase the polarization character of AlN, which in turn increases the dielectric constant. This is contrast to Al vacancies, which reduce the polarization and lead to a decrease in the dielectric constant. Although excess Al atoms can increase the number of free electrons and thus reduce the dielectric constant, the high dielectric constant suggests a larger contribution of the former mechanism.
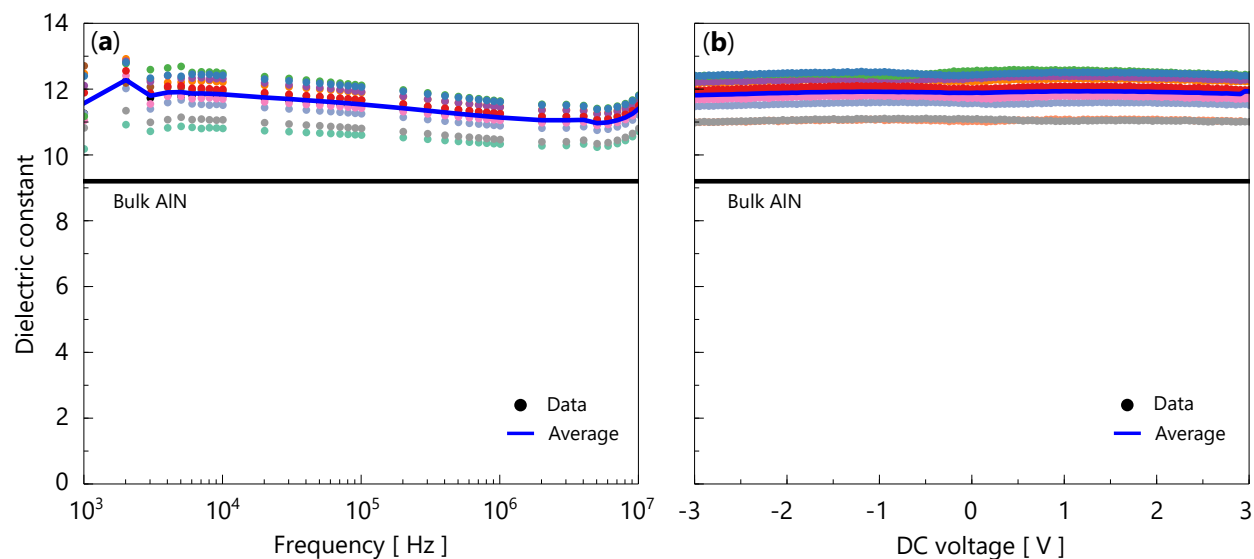
Figure S6. Electrical breakdown tests conducted as functions of (a) frequency and (b) voltage. The AlN deposition for these tests was performed on top of a film of Pt which was deposited on a thermal SiO_2-Si substrate. Each set of colored circles represents measurements performed on a different 'dot' of Pt. The average dielectric constant from these measurements ranged from 11.5-11.9.

References

1. Yalon, E. *et al.* Temperature-dependent thermal boundary conductance of monolayer mos2 by raman thermometry. *ACS Applied Materials Interfaces* **9**, 43013–43020 (2017). DOI 10.1021/acsami.7b11641.

2. Kwon, H., Perez, C., Park, W., Asheghi, M. & Goodson, K. E. Thermal characterization of metal–oxide interfaces using time-domain thermoreflectance with nanograting transducers. *ACS Applied Materials Interfaces* **13**, 58059–58065 (2021). DOI 10.1021/acsami.1c12422.

3. Perez, C. *et al.* Dominant energy carrier transitions and thermal anisotropy in epitaxial iridium thin films. *Advanced Functional Materials* **2207781**, 1–9 (2022). DOI 10.1002/adfm.202207781.

4. Giauque, W. F. & Meads, P. F. The heat capacities and entropies of aluminum and copper from 15 to 300°k. *Journal American Chemical Society* **63**, 1897–1901 (1941). DOI 10.1021/ja01852a027.

5. Gaskins, J. T. *et al.* Review—Investigation and Review of the Thermal, Mechanical, Electrical, Optical, and Structural Properties of Atomic Layer Deposited High- k Dielectrics: Beryllium Oxide, Aluminum Oxide, Hafnium Oxide, and Aluminum Nitride. *ECS Journal Solid State Science Technology* **6**, N189–N208 (2017). DOI 10.1149/2.0091710jss.

6. E.H. Touloukian, Y. & Buyco. *Thermophysical properties of matter - the TPRC data series. Volume 5. Specific heat - nonmetallic solids. (Reannouncement). Data book* (1970).

7. Yang, J., Ziade, E. & Schmidt, A. J. Uncertainty analysis of thermoreflectance measurements. *Review Scientific Instruments* **87**, 1–11 (2016). URL http://dx.doi.org/10.1063/1.4939671. DOI 10.1063/1.4939671.

8. Little, W. The transport of heat between dissimilar solids at low temperatures. *Canadian Journal Physics* **37**, 334–349 (1959).

9. Swartz, E. T. & Pohl, R. O. Thermal boundary resistance. *Reviews Modern Physics* **61**, 605–668 (1989). DOI 10.1103/RevModPhys.61.605.

10. Schwoerer-Böhning, M., Macrander, A. T., Pabst, M. & Pavone, P. Phonons in wurtzite aluminum nitride. *Physica Status Solidi (B) Basic Research* **215**, 177–180 (1999). DOI 10.1002/ (SICI)1521-3951(199909)215:1<177::AID-PSSB177>3.0.CO;2-8.

11. Dutton, D. H. & Brockhouse, B. N. Crystal dynamics of platinum by inelastic neutron scattering. *The Canadian Journal Physics* **50**, 422–422 (1972). DOI 10.1177/070674377902400508.

12. Koh, Y. R. *et al.* High thermal conductivity and thermal boundary conductance of homoepitaxially grown gallium nitride (gan) thin films. *Physical Review Materials* **5** (2021). DOI 10.1103/PhysRevMaterials.5.104604.

13. Cheng, Z. *et al.* Thermal conductance across harmonic-matched epitaxial al-sapphire heterointerfaces. *Communications Physics* **3** (2020). DOI 10.1038/s42005-020-0383-6.

14. Monachon, C., Weber, L. & Dames, C. Thermal boundary conductance: A materials science perspective. *Annual Review Materials Research* **46**, 433–463 (2016). DOI 10.1146/annurev-matsci-070115-031719.

15. Callaway, J. Model for lattice thermal conductivity at low temperatures. *Physical Review* **113**, 1046–1051 (1959). DOI 10.1103/PhysRev.113.1046.

16. Liu, W. & Balandin, A. A. Thermal conduction in alxga1-xn alloys and thin films. *Journal Applied Physics* **97** (2005). DOI 10.1063/1.1868876.

17. Yi, S. I. & Yu, C. Modeling of thermoelectric properties of sige alloy nanowires and estimation of the best design parameters for high figure-of-merits. *Journal Applied Physics* **117** (2015). DOI 10.1063/1.4906226.

18. Yi, S. I. *et al.* Strain-induced suppression of the miscibility gap in nanostructured mg2si-mg2sn solid solutions. *Journal Materials Chemistry A* **6**, 17559–17570 (2018). DOI 10.1039/c8ta05798b.

19. Xu, R. L. *et al.* Thermal conductivity of crystalline AlN and the influence of atomic-scale defects Thermal conductivity of crystalline AlN and the in fl uence of atomic-scale defects. *Journal Applied Physics* **126**, 1–7 (2019). DOI 10.1063/1.5097172.

20. Morelli, D. T., Heremans, J. P. & Slack, G. A. Estimation of the isotope effect on the lattice thermal conductivity of group iv and group iii-v semiconductors. *Physical Review B - Condensed Matter Materials Physics* **66**, 1953041–1953049 (2002). DOI 10.1103/PhysRevB.66.195304.

21. Bruls, R. J., Hintzen, H. T., With, G. D., Metselaar, R. & Miltenburg, J. C. V. The temperature dependence of the gruneisen parameters of mgsin2, aln and -si3n4. *Journal Physics Chemistry Solids* **62**, 782–792 (2001). URL www.elsevier.nl/locate/jpcs.

22. Nilsson, D., Janzén, E. & Kakanakova-Georgieva, A. Lattice parameters of aln bulk, homoepitaxial and heteroepitaxial material. *Journal Physics D: Applied Physics* **49** (2016). DOI 10.1088/0022-3727/49/17/175108.

23. Slack, G. A., Tanzilli, R., Pohl, R. & Vandersande, J. The intrinsic thermal conductivity of aln. *Journal Physics Chemistry Solids* **48**, 641–647 (1987). URL https://www.sciencedirect.com/science/article/pii/0022369787901533. DOI https://doi.org/10.1016/0022-3697(87)90153-3.

24. Gaddy, B. E. *et al.* The role of the carbon-silicon complex in eliminating deep ultraviolet absorption in aln. *Applied Physics Letters* **104** (2014). DOI 10.1063/1.4878657.